Tectonophysics 753 (2019) 93–110

Contents lists available at ScienceDirect

Tectonophysics

journal homepage: www.elsevier.com/locate/tecto

Receiver function analysis reveals layered anisotropy in the crust and upper mantle beneath southern Peru and northern Bolivia

Neta Bar[a,*], Maureen D. Long[a], Lara S. Wagner[b], Susan L. Beck[c], George Zandt[c], Hernando Tavera[d]

[a] Department of Geology and Geophysics, Yale University, PO Box 208109, New Haven, CT 06520, USA
[b] Department of Terrestrial Magnetism, Carnegie Institution for Science, 5241 Broad Branch Rd. NW, Washington, DC 20015, USA
[c] Department of Geosciences, University of Arizona, 1040 East 4th St., Tucson, AZ 85721, USA
[d] Instituto Geofisico del Peru, Calle Badajoz 169, Lima 15012, Peru

ARTICLE INFO

Keywords:
Receiver function
Seismic Anisotropy
Southern Peru
Northern Bolivia
Crustal deformation
Andes

ABSTRACT

Subduction systems play a key role in plate tectonics, but the deformation of the crust and uppermost mantle during continental subduction remains poorly understood. Observations of seismic anisotropy can provide constraints on dynamic processes in the crust and uppermost mantle in subduction systems. The subduction zone beneath Peru and Bolivia, where the Nazca plate subducts beneath South America, represents a particularly interesting location to study subduction-related deformation, given the along-strike transition from flat to normally dipping subduction. In this study we constrain seismic anisotropy within and above the subducting slab (including the overriding plate) beneath Peru and Bolivia by examining azimuthal variations in radial and transverse component receiver functions. Because anisotropy-aware receiver function analysis has good lateral resolution and depth constraints, it is complementary to previous studies of anisotropy in this region using shear wave splitting or surface wave tomography. We examine data from long-running permanent stations NNA (near Lima, Peru) and LPAZ (near La Paz, Bolivia), and two dense lines of seismometers from the PULSE and CAUGHT deployments in Peru and Bolivia, respectively. The northern line overlies the Peru flat slab, while the southern line overlies the normally dipping slab beneath Bolivia. We applied harmonic decomposition modeling to constrain the presence, depth, and characteristics of dipping and/or anisotropic interfaces within the crust and upper mantle. We found evidence for varying multi-layer anisotropy, in some cases with dipping symmetry axes, underneath both regions. The presence of multiple layers of anisotropy with distinct geometries that change with depth suggests a highly complex deformation regime associated with subduction beneath the Andes. In particular, our identification of depth-dependent seismic anisotropy within the overlying plate crust implies a change in deformation geometry, dominant mineralogy, and/or rheology with depth, shedding light on the nature of deep crustal deformation during orogenesis.

1. Introduction

The subduction of the Nazca Plate beneath Peru and Bolivia encompasses a major along-strike change in slab morphology and overriding plate behavior (e.g., Antonijevic et al., 2015; Gutscher et al., 1999, 2000; Kumar et al., 2016; Scire et al., 2016). The Central Andean Plateau, the second-highest plateau on Earth, overlies normally dipping subduction beneath the central portion of South America. Just to the north of this region lies the Peru flat slab segment, which is characterized by a striking lack of contemporary volcanism and low heat flow on the overriding plate. The controls on this dramatic along-strike change in slab behavior, as well as the corresponding along-strike change in topographic expression on the overriding plate, remain poorly known. Furthermore, it is not well understood how the crust has deformed during orogenesis, and to what extent the deformation style of the overriding plate is controlled by the morphology and behavior of the subducting slab beneath it (e.g., Bishop et al., 2018).

Observations of seismic anisotropy can provide important constraints on the deformation history of the crust and mantle in subduction systems (e.g., Long, 2013). Seismic anisotropy is the dependence of seismic wave speeds on the propagation direction or polarization of the waves (e.g., Silver and Chan, 1991). Seismic anisotropy often forms due to deformation either through crystallographic or lattice preferred orientation (CPO, LPO) of minerals or as shape preferred orientation (SPO) of materials of certain elastic properties (Savage, 1999). While shear wave splitting or birefringence is a direct and unequivocal sign of anisotropy, the interpretation is often complicated, especially in regions of complex

---

* Corresponding author.
E-mail address: neta.bar@yale.edu (N. Bar).

https://doi.org/10.1016/j.tecto.2019.01.007
Received 6 July 2018; Received in revised form 11 January 2019; Accepted 17 January 2019

anisotropic structure (e.g., Long and Becker, 2010). A number of detailed shear wave splitting studies have recently been published for southern Peru and northern Bolivia (Eakin and Long, 2013; Eakin et al., 2014, 2015; Long et al., 2016), shedding light mainly on upper mantle anisotropy, but their interpretation is somewhat ambiguous because shear wave splitting measurements generally lack depth resolution.

Receiver functions (RFs), on the other hand, provide information regarding sharp seismic velocity gradients (both isotropic and anisotropic) beneath a seismic station, and have been used extensively to study anisotropic crustal and mantle structures (e.g., Bostock, 1998; Ford et al., 2016; Levin and Park, 1997; Long et al., 2017; Schulte-Pelkum and Mahan, 2014; Shiomi and Park, 2008; Wirth and Long, 2012, 2014; Wirth et al., 2017). RFs can constrain some anisotropic structural features that are not easily inferred from other methods such as shear wave splitting or surface wave tomography. For example, RFs can help constrain the depth extent of anisotropic layers and the orientation of symmetry axes (e.g., Wirth and Long, 2012). In a subduction system such as central South America, RFs analysis can provide constraints on crustal deformation and mantle flow that are complementary to shear wave splitting studies (e.g., McCormack et al., 2013; Park et al., 2002, 2004; Shiomi and Park, 2008; Wirth and Long, 2012).

This study aims to constrain seismic anisotropy beneath Peru and Bolivia using anisotropic radial and transverse component receiver function analysis. We focus on data from two long-running seismic stations: NNA, near Lima, Peru, and LPAZ, near La Paz, Bolivia. We also examine data from two complementary temporary deployments: PULSE (PerU Lithosphere and Slab Experiment) in Peru and CAUGHT (Central Andes Uplift and Geodynamics of High Topography) in Bolivia (Fig. 1). Our goal is to place constraints on seismic anisotropy and its distribution with depth both within and above the slab, including the mantle wedge and the overriding plate. We apply a harmonic decomposition modeling technique (e.g., Bianchi et al., 2010; Ford et al., 2016; Long et al., 2017; Olugboji and Park, 2016) to our computed RFs to identify the depths and first-order characteristics of anisotropic and/or dipping interfaces beneath our seismic stations, and compare those inferences to previous studies of anisotropy from shear wave splitting and anisotropic Rayleigh wave tomography from the same region and data set.

2. Geologic and tectonic setting

The Central Andes above the subducting Nazca plate in northern Bolivia and southern Peru are characterized by a striking change from a narrow orogen in the north to the second-highest plateau on Earth in the south (e.g., Lamb and Hoke, 1997). The Central Andean Plateau, a relatively flat plateau with an average elevation of ~3.5 km (Isacks, 1988; McQuarrie et al., 2008), overlies normally dipping subduction beneath the central portion of South America (e.g., Hayes et al., 2012). Its edges consist of an active volcanic arc to the west (Western Cordillera) and a fold and thrust belt to the east (eastern Cordillera). The origin of the plateau's high topography is imperfectly understood and may result from processes both in the crust and the mantle wedge (e.g., Garzione et al., 2006, 2008, 2017). The seaward concave bend in the Andes at this latitude is another prominent feature in this region.

Just to the northwest of the Central Andean Plateau lies the Peruvian flat slab segment, which is characterized most strikingly by a lack of present-day volcanism. The Peruvian flat slab is the largest region of flat subduction in the world today and is also associated with low heat flow and broad foreland uplift (Bishop et al., 2017; Cahill and Isacks, 1992; Eakin et al., 2014; Hayes et al., 2012). Previous studies on flat subduction have argued that flat slabs lead to compressional crustal deformation and thickening in the upper plate (e.g., Bishop et al., 2018; Erslev, 2005; Jordan and Allmendinger, 1986). The structure and deformation of the crust and mantle wedge above this flat slab can provide us with important insights into the relationship between the flat slab and the overriding continent, and contribute to our understanding of the surface expression of flat subduction as well. Taken together, the Peruvian flat slab segment and the adjacent normally dipping slab beneath the high plateau represent an excellent opportunity to probe how the along-strike change in slab dip may affect deformation patterns within the mantle above the slab as well as the crust of the overriding plate.

3. Data and methods

Receiver functions are time series, computed from three-component seismograms, that show the relative response of Earth structure near the receiver. When a P wave encounters an isotropic, horizontal velocity discontinuity at depth, it will convert to an SV-wave, with a polarity that reflects the sign of the velocity contrast (either positive, corresponding to a velocity increase with depth, or negative, corresponding to a velocity decrease with depth). In the presence of an anisotropic or a dipping interface, however, the P wave will also produce an additional SH wave, which will be visible on the transverse component (Levin and Park, 1997). Note that here we use the common terminology of SV and SH polarizations to described shear waves polarized in the source-receiver

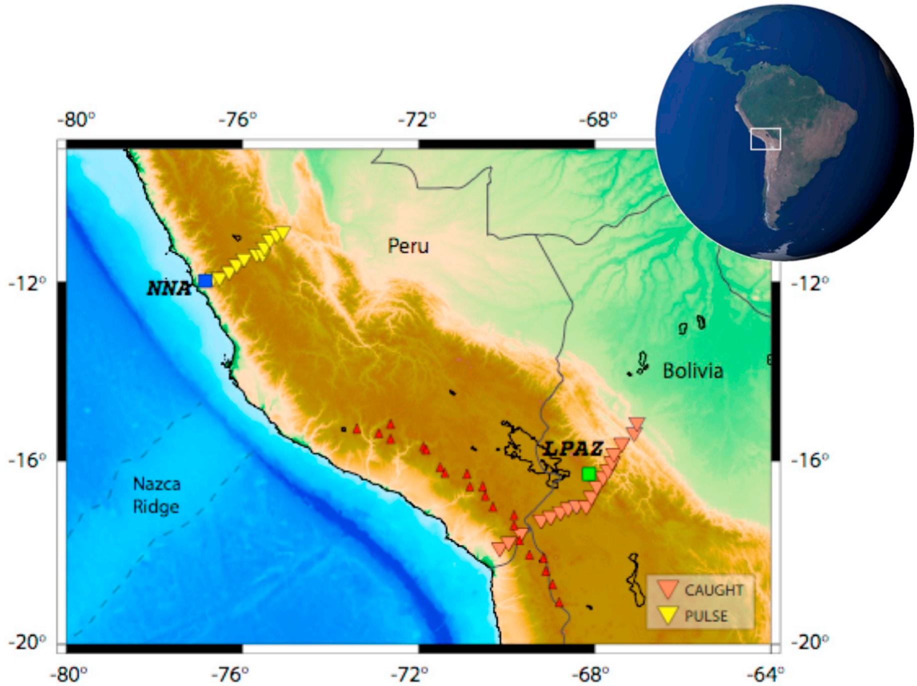

Fig. 1. Station map showing locations of NNA (blue square) and LPAZ (green square) along with the dense lines of CAUGHT (orange triangles) and PULSE (yellow triangles). Inset map shows location of our study area (white box) along the South American subduction zone. Red triangles mark Quaternary volcanic zones (Mamani et al., 2010). Note that the lack of volcanism in northern and central Peru corresponds with the flat slab. (For interpretation of the references to colour in this figure legend, the reader is referred to the web version of this article.)

plane (SV, radial component) and orthogonal to it (SH, transverse component), following Levin and Park (1997) and others. Because we are measuring nearly vertically propagating shear waves, both SV and SH waves involve nearly horizontal particle motion, and are measured on the horizontal components of the seismogram.

In general, a dipping interface will result in two polarity changes (two-lobed) of the Ps phase (that is, the P to S converted wave) on the transverse component receiver function across the full backazimuthal range. A flat interface with a horizontal anisotropy symmetry axis, in contrast, will result in four polarity changes (four-lobed) across the full backazimuthal range (e.g., Ford et al., 2016; Levin and Park, 1997; Wirth and Long, 2012). More complicated patterns may be produced in the case of an anisotropic interface that involves a plunging axis of symmetry; in this case, the backazimuthal pattern may reflect a mix of two-lobe and four-lobe polarity changes. In theory, there are several ways to distinguish conversions due to a dipping (isotropic) interface from those associated with gradients in anisotropy with a plunging symmetry axis (e.g., Jones and Phinney, 1998; Long et al., 2017; Savage, 1998; Schulte-Pelkum and Mahan, 2014), although in practice this is often challenging for real data (Long et al., 2017). One common strategy is to examine energy at zero-delay time ($t = 0$) on the transverse RF. A dipping isotropic contrast should generate a matching arrival at zero time that has polarities opposite of those for the later arrival corresponding to the interface depth (see, e.g., Schulte-Pelkum and Mahan, 2014 for a detailed discussion). The zero-delay time arrival corresponds to the refracted direct P wave energy, while the later arrival is the converted Ps wave. For a contrast with anisotropy at depth with a plunging symmetry axis, there will be no zero-delay time arrival on the transverse component. An important caveat, however, is that for real data that contains conversions from multiple interfaces at depth, this approach is not straightforward, as multiple zero-time arrivals may interfere.

We computed P-to-S RFs at two long-running broadband seismic stations: NNA from the Global Seismograph Network (near Lima, Peru) and LPAZ from the Global Telemetered Seismic Network (near La Paz, Bolivia). We also computed RFs at stations from two temporary dense lines of two seismic arrays: the PULSE experiment and the CAUGHT experiment, in southern Peru and Northern Bolivia, respectively. We chose stations along two SW-NE transects that encompass NNA (11 stations from PULSE) and LPAZ (17 stations from CAUGHT) (Fig. 1). Waveform data were downloaded from the Incorporated Research Institutions for Seismology (IRIS) Data Management Center (DMC) using the Standing Order for Data (SOD) tool (Owens et al., 2004). We selected events of magnitude 5.8 and greater from epicentral distances between 30° and 100° (Fig. 2) for initial analysis. The number of events ultimately used at each station depends on the number of years of available data (more than ten years' worth of data from the permanent stations and between 22 and 32 months for the temporary stations) as well as station noise levels and general waveform quality.

Our data selection and preprocessing methodology follows recent studies that have applied RF analysis to study seismic anisotropy (Ford et al., 2016; Long et al., 2017; Wirth and Long, 2012, 2014). More specifically, we directly followed the preprocessing procedure that is described by Ford et al. (2016): each seismogram trace was cut to equal length, rotated into radial, transverse, and vertical components, and then bandpass filtered between 0.02 and 2 Hz before P wave picking. The seismograms were visually inspected for a clear P wave arrival on the vertical component, and the direct P arrival was manually picked using the Seismic Analysis Code (SAC). Before computing the RFs, the components were rotated into the LQT reference frame (using a near-surface P wave velocity of 3.5 km/s) to address the fact that the incoming P waves are not perfectly vertical, again following Ford et al. (2016). We note that without detailed knowledge of the near-surface velocity structure, this correction is imperfect, and some energy from the direct P arrival will be visible on the Q component. Since all RFs were computed in the LQT coordinate system, instead of the common terminology of "radial" RFs (e.g., Levin and Park, 1997) we use the term "quasi-radial" to refer to the Q component in this paper. Finally, before the RF computation, we applied a final bandpass filter to each waveform, using a high pass cutoff of 0.02 Hz and variable low pass cutoffs of 0.5, 0.75, 1 and 2 Hz. In this paper, we mainly focus on results obtained using the 1 Hz low pass cutoff frequency, as this provided the best balance between revealing detailed structure and removing unwanted noise.

We calculated P-to-S RFs using the multi-taper correlation RF estimator of Park and Levin (2000), in which the receiver functions are calculated in the frequency domain from the correlation between the vertical component and each of the horizontal components. We used a one-dimensional velocity model appropriate for continents (AK135; Kennett et al., 1995) to migrate RFs to depth. Since our major focus is on identifying the character of anisotropic interfaces rather than their precise depth, our migration analysis does not account for departures from the AK135 crustal model, which may be significant in our study area due to the high topography. Previous studies of (isotropic) structure beneath the PULSE and CAUGHT study areas have used more detailed crustal models to estimate interface depths, and we refer the reader to this previous work (Bishop et al., 2017; Ryan et al., 2016). We do, however, correct for elevation in our estimated depths to interfaces. Following recent work (Ford et al., 2016; Long et al., 2017), we computed binned, stacked quasi-radial and transverse component RFs as a function of epicentral distance and backazimuth. The epicentral distance gather helps us evaluate the possible effects of multiply reflected waves on our results (specifically, multiply reflected arrivals will have a strong moveout with epicentral distance). The backazimuth gather, particularly the transverse component, helps to visually identify potential dipping and/or anisotropic interfaces. Additionally, we have produced a single-station quasi-radial component RF stack (following Ford et al., 2016) by first binning RFs as a function of backazimuth using a bin spacing of 15°, and summing over all bins to produce a stack. Because we first bin data by backazimuth, the resulting stack should not be biased towards backazimuths with better azimuthal coverage. The single station binned-stacks help us to identify major (isotropic) velocity contrasts, both positive and negative, and allow for comparison with previous RF studies using PULSE and CAUGHT data (Bishop et al., 2017; Ryan et al., 2016).

In addition to the RF stacks and epicentral distance and backazimuthal gathers, we plotted rose diagrams (Wirth and Long, 2014) that visualize variations in the transverse component RFs energy as a function of backazimuth for a specific delay time (corresponding to a specific depth). This plotting convention illustrates the polarity (red—negative, blue—positive) and amplitude (darker colors indicate higher amplitude) for a particular back azimuth, and helps identify two-lobed, four-lobed, or a mixture of polarity changes which relate to the type of interface (dipping, anisotropic or both).

As a final step, we also implemented harmonic decomposition (HD) analysis (Bianchi et al., 2010; Ford et al., 2016; Liu and Park, 2016; Long et al., 2017; Olugboji and Park, 2016; Park and Levin, 2016; Shiomi and Park, 2008), an approach that can help to overcome limitations of visual identification of amplitude and polarity changes as a function of backazimuth. The harmonic expansion reveals two-lobed and four-lobed backazimuthal dependence by performing a linear regression of both radial and transverse RFs components. The analysis determines the amplitudes at each delay time as a scaled sum of $\cos(k\phi)$ and $\sin(k\phi)$ terms; here k, the harmonic order, is equal to 0,1,2, and ϕ refers to the backazimuth. The isotropic velocity contrast (constant term) is represented by $k = 0$, while $k = 1$ and $k = 2$ correspond to the two-lobe and four-lobe patterns (non-constant terms), respectively. The $k = 1$ term contains information on the dip direction of either a dipping interface or a plunging anisotropic symmetry axis, whereas the $k = 2$ term contains azimuthal phase information on the orientation of symmetry axis for the contrast in azimuthal anisotropy. (We note that while a non-zero $k = 2$ term suggests the presence of anisotropy, the relative amount of $k = 1$ vs. $k = 2$ energy on the stack will depend on the details of the anisotropic geometry, as expressed via parameters such as the shape factor; see Brownlee et al., 2017 for additional details.) To reveal the signal of anisotropy or dipping interfaces, we stack the radial and transverse RFs with a phase shift ($+\pi/$

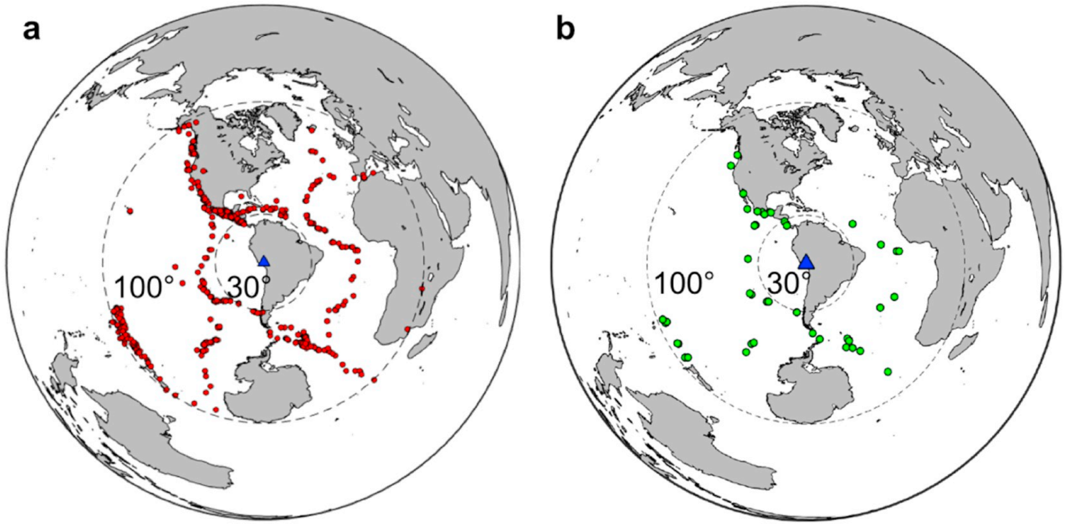

Fig. 2. Maps of events used for RF analysis in this study. Study region marked by the blue triangle. Black lines mark the epicentral distance limits of 30° and 100°. (a) Events for all stations (including LPAZ, NNA and the subset of the temporary stations from the CAUGHT and PULSE deployments) that yielded at least one usable RF are marked by the red circles. (b) An example of the event distribution used for one of the temporary stations (green circles); this example is from station CB28 from the CAUGHT deployment. Note the considerably poorer azimuthal coverage, as compared to the dataset as a whole. (For interpretation of the references to colour in this figure legend, the reader is referred to the web version of this article.)

2 k) in backazimuth, producing the 'modeled' plot. In contrast, stacking the radial and transverse RFs with a negative phase shift ($-\pi/2$ k) results in the 'unmodeled' panel, in which effects of anisotropy or dipping structures are suppressed (Liu and Park, 2016). A complete description of the HD modeling approach is found in both Bianchi et al. (2010) and Liu and Park (2016), and a detailed implementation of the HD method, with examples, is given in Ford et al. (2016).

The RF harmonic regression was performed with a moveout correction for a specific target depth via the moving-window migration (MWM) technique, in which we cross-correlate the vertical component with horizontals with a time delay related to target depth (Helffrich, 2006; Park and Levin, 2016). Because the MWM approach yields a time series that is most accurate for a range of ~10–15 km around the target depth (e.g., Park and Levin, 2016), we implemented HD analysis for a series of target depths ranging from 20 to 100 km in 10 km steps to obtain a model that is as accurate as possible for each depth range of interest. This approach provides a point of comparison for our inferences on isotropic structure from the single-station quasi-radial RF stacks, and allows us to explore signals of anisotropic interfaces that are not evident from visual inspection in the RFs stacks.

Our presentation of the HD results in this paper focuses on specific target depths close to where we detect major interfaces, either through significant peaks in the single-station RF stacks, in the constant term (k = 0) of the HD analysis, and/or in the stack of the non-constant terms (reflecting significant contract in anisotropy or a dipping interface). In the HD model plots, $t = 0$ on the time axis corresponds to the RF behavior at the time associated with the target depth under consideration, following plotting conventions used in previous papers (e.g., Ford et al., 2016). The uncertainties on the harmonic decomposition models were estimated using a bootstrap method (100 iterations). Bootstrapping is a resampling technique that allows for error estimation for nonlinear problems (e.g., Menke, 2012); it has many advantages for RF studies (e.g., Park and Levin, 2016), although it may be inaccurate for cases in which the number of observations is small.

In addition to the HD plots themselves, we also computed several examples of comparisons between the modeled transverse component (based on the HD results) and transverse component rose plots; these comparisons illustrate the good fit between the HD analysis and the RF observations. Based on the HD expansion, we calculated estimated directions of the tilt axis associated with specific interfaces (see, e.g., Long et al., 2017; Olugboji and Park, 2016). For a slow-over-fast interface, a positive pulse in the sin(ϕ) term reflects an east (90°) direction whereas a negative pulse reflects the opposite (west) direction; likewise, a positive pulse in the cos(ϕ) term reflects north (0°) direction and a negative pulse reflect the opposite (south) direction. Based on the sign of the k = 0 pulse amplitude (positive or negative) and the relative amplitudes of each k = 1 term, we can thus calculate the estimated tilt axis. We note that for an isotropic dipping interface, we can determine the dip direction based on information from the quasi-radial component, which reflects either a positive arrival (slow-over-fast) or a negative arrival (fast-over-slow). On the other hand, for a plunging symmetry axis we cannot discriminate the direction of the plunge; therefore, we present both directions as potential options.

4. Results

Results of our RF analysis and HD modeling are displayed in Figs. 3 to 11 and include binned and stacked quasi-radial and transverse component RFs as a function of backazimuth (low pass cutoff frequency of 1 Hz), binned and stacked quasi-radial RFs as a function of epicentral distance, results from the HD modeling, single station binned-stacks for the quasi-radial RF component, and rose plots for specific time delays that show evidence for dipping and/or anisotropic interfaces. We also show RF gathers computed with a range of low pass cutoff frequencies in the supplementary information (Figs. S1-S2). We have validated our quasi-radial RF results against the results of previous work in Bolivia (Ryan et al., 2016) and Peru (Bishop et al., 2017) using data from the same stations but different methodologies for computing and stacking the RF traces. Specifically, our observation of high amplitudes of positive arrivals at or near depths predicted by previous work has helped us to identify both the continental Moho and the subducting slab Moho (beneath NNA) interfaces, as discussed below. Because we explicitly take azimuthal dependence of RF behavior into account, however, our approach offers additional spatial and azimuthal resolution of features that were identified in these earlier papers. Other RF features identified in the single-station binned quasi-radial stack and the HD modeling represent evidence for intra-crustal and mantle structures that likely include anisotropic contrasts, as discussed below.

4.1. Station LPAZ, Bolivia

LPAZ is deployed on the Eastern Cordillera at elevation of ~5 km above sea level, located above the normally dipping slab beneath the

Central Andean Plateau (Fig. 1). The depth to the slab beneath LPAZ is roughly 300 km, based on tomographic imaging of the slab in the deep upper mantle (Scire et al., 2016). Fig. 3 shows the results of our RF analysis for the Moho interface beneath LPAZ and illustrates the plotting conventions we use in this paper. In Fig. 3a, we show the quasi-radial and transverse component RFs as a function of backazimuth; these plots help us identify major interfaces with a strong isotropic component (mostly the Moho) on the quasi-radial component, as well as potentially dipping and/or anisotropic interfaces on the transverse component. Fig. 3b shows the quasi-radial component RFs binned and stacked as a function of epicentral distance, which helps us to evaluate the possible effects of multiply reflected waves. Fig. 3c presents the single-station binned stack for the quasi-radial component RF, which helps identify (isotropic) velocity contrasts that manifest across a wide range of backazimuths, and also allows for direct comparison with previous RF studies that have used this stacking approach. Fig. 3d shows an example of a transverse component rose diagram (in this case for the delay time associated with the Moho interface); this allows us to

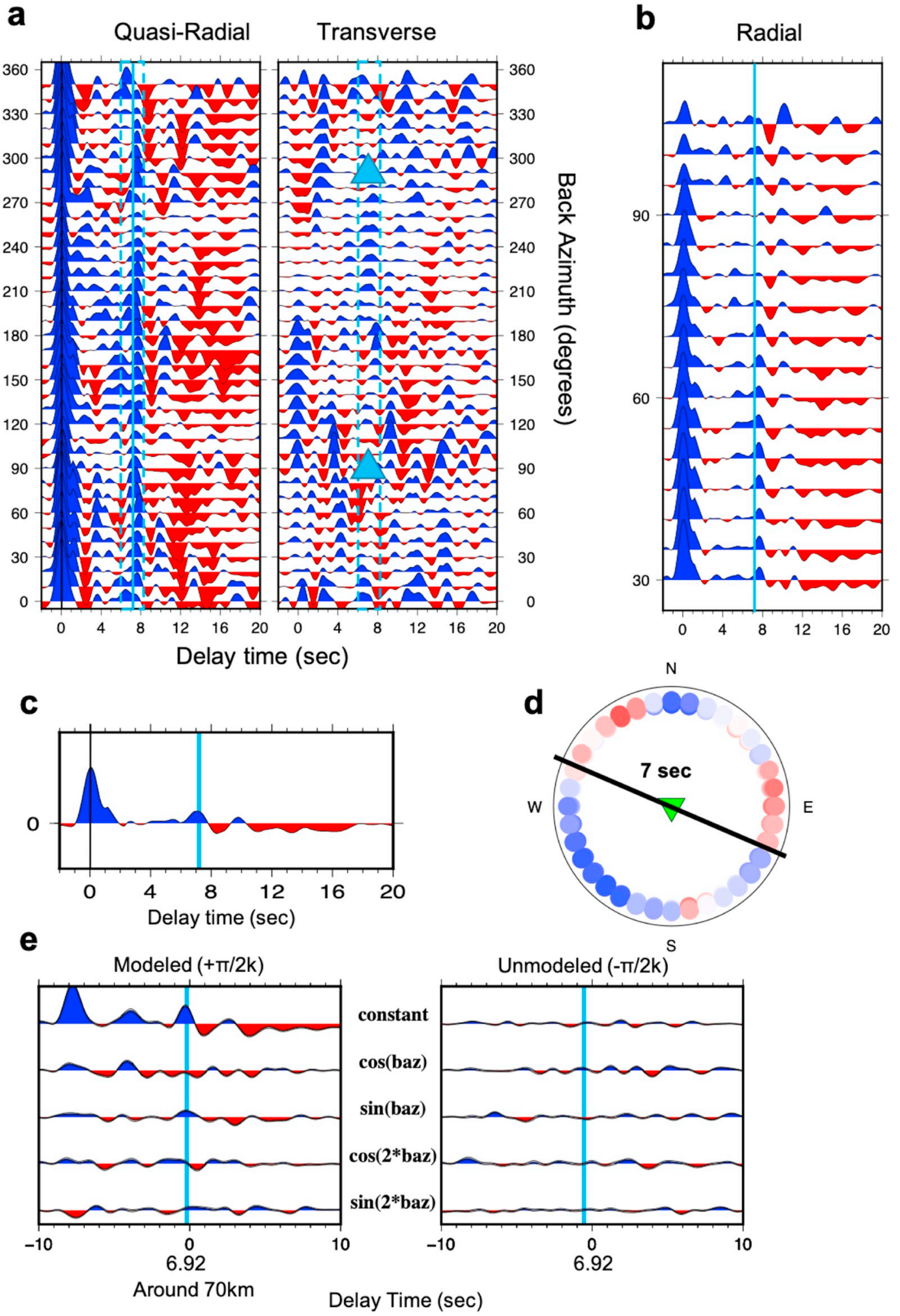

(caption on next page)

Fig. 3. Results of our RF analysis at station LPAZ, with an emphasis on characterizing the Moho arrival. (a) Quasi-radial (left) and transverse (right) component RFs that have been migrated, gathered in backazimuthal bins (as indicated on y axis), and stacked. Arrivals in blue correspond to pulses with the same polarity as the main P wave pulse, generally indicating a velocity increase with depth, while arrivals in red correspond to pulses with the opposite polarity. The cyan dashed lines on both the radial and transverse RF gathers mark the time range within which we observe a converted arrival from the Moho interface range. The solid cyan line marks the best guess at the Moho pick. The blue triangles on the transverse component mark the azimuths at which we see a (two-lobed) change in polarity. (b) Stacked quasi-radial component RFs, gathered as a function of epicentral distance (as indicated on y axis). (c) Binned-stack of all quasi-radial component RFs, over all backazimuths and epicentral distances. The cyan line marks the Moho pick. (d) Rose plot of the transverse component RF amplitude over the time range corresponding to the Moho pick, showing the azimuthal variability in amplitude. Colour convention is the same as in (a), with positive pulses in blue and negative pulses in red. The rose plot amplitudes were normalized such that the maximum amplitude in the plot is equal to 1. The black line marks the inferred tilt axis direction (~112° or ~292°) of the Moho interface based on HD direction analysis, as described in the text. (e) Harmonic decomposition results, computed around a target depth (~70 km) corresponding to the Moho pick, along with their minimum and maximum bootstrap error estimates. (Note that because of the large number of RFs available at this station, the bootstrap error bounds are virtually indistinguishable from the trace.) We show the modeled ($+\pi/2\,k$) portion of the HD on the left, with the top trace corresponding to the k = 0 (constant) term, the next two traces corresponding to the k = 1 terms, and the final two traces corresponding to the k = 2 terms. The right panels show the unmodeled or suppressed ($-\pi/2\,k$) portion of the HD. Beneath each time axis, we show the center time associated with the target depth (in *sec*) beneath the $t = 0$ reference time. The cyan line marks the Moho in each component (near a delay time of zero sec on the x axis; here a zero sec delay time corresponds to the expected arrival time for a conversion at the target depth). (For interpretation of the references to colour in this figure legend, the reader is referred to the web version of this article.)

visualize variations in the transverse component RF energy as a function of backazimuth at a particular delay time. Such rose plots visually illustrate two-lobed or four-lobed polarity changes (or a mixture of these) that relate to a specific interface. Finally, Fig. 3e presents the HD model for a target depth corresponding to the Moho arrival; we plot both the HD model itself and its bootstrap uncertainty estimates. (Note that for this station, the large number of RFs available means that the bootstrap error estimates are virtually indistinguishable from the trace itself.) The HD model plot shows the HD expansion of the different cos (kϕ) and sin(kϕ) terms, with the k = 0 term in the top trace, the k = 1 terms in the next two traces, and the k = 2 terms in the bottom two traces. Examples of comparisons between the modeled transverse component rose plots using the results of the HD analysis and actual observed transverse component rose plots from the RF data are shown in Fig. 4 (panel b), and illustrate the remarkably good fit between the "raw" RF observations and the HD analysis.

The quasi-radial component RF gathers for LPAZ (Fig. 3a), along with the single-station binned stack (Fig. 3c), reveal a clear strong positive pulse between 6 and 8 s after the P wave arrival, with a peak at 7 s (shown most clearly in the single-station stack). We interpret this feature as a positive isotropic velocity change across the Moho. This time interval corresponds to ~60–70 km crustal thickness beneath Bolivia based on the AK135 velocity model, taking into account the LPAZ station elevation. The transverse component (Fig. 3a) shows two polarity changes across the full backazimuthal range around the time interval of the positive Moho pulse on the quasi-radial component. This dominantly 2-lobed pattern is clearly visible in the rose diagrams for 7 s delay time (Fig. 3d), although it seems to be modulated by an additional 4-lobed pattern, suggesting a component of anisotropy. The transverse component RFs exhibit substantial energy at the zero-delay time, but the polarity pattern does not match what would be expected for this interface if it is dipping. This observation may suggest a contrast in plunging anisotropy rather than isotropic dipping interface (although caution is warranted when interpreting zero-time energy for stations that overlie multiple interfaces). Furthermore, the harmonic decomposition approach (Fig. 3e) also suggests an interface in this time (depth) range, with a positive amplitude in the constant term and a consistent high amplitude in the combined non-constant terms. The significant amplitude in the non-constant terms appears mostly in the k = 1 terms, (particularly in sin(ϕ)), with some (lower amplitude) energy in the k = 2 terms. Taken together, the 2-lobe pattern and the HD analysis suggest either a dipping crust-mantle interface with some anisotropy, or anisotropic interface with a plunging symmetry axis. As explained in Section 3, we can calculate an estimated tilt axis associated with a specific interface based on the HD expansion terms. For the interface associated with the Moho beneath LPAZ, we calculated an estimated tilt direction of ~112°/292° (the two possible (opposite) directions of the tilt, in degrees east of north), which agrees well with the visual characteristics of the rose plot diagram.

In addition to the Moho, we see evidence in the single-station binned-stack, as well as in the HD analysis, for additional interfaces represented by peaks of energy marking isotropic and/or anisotropic structures. We have chosen high amplitude peaks both in the single-station stacks and HD (constant and non-constant terms), based on a relative amplitude cut off of 30% of the Moho peak amplitude (we chose a fraction of the Moho peak, as it is a robust feature in our analysis and well known from previous studies). The non-constant terms were added together, following Ford et al. (2016), to provide a quantitative way of identifying interfaces with an anisotropic component. (To reiterate, the single-station and HD constant term (k = 0) both represent interfaces that include a component of isotropic impedance contrast.) This analysis revealed 7 different interfaces beneath LPAZ that we consider to be interpretable. Some of these interfaces are within the crust, and some are within the lithospheric mantle; most of these interfaces exhibit a mix of isotropic and anisotropic contrasts.

The intracrustal features beneath LPAZ include four interfaces; two of them reflect both isotropic and anisotropic signal, whereas the other two reflect mostly anisotropic signal. The first interface is a large positive pulse at 1.2–1.5 s after the P arrival that is visible in the single-station stack (Fig. 4a) and the k = 0 term of the HD (Fig. 5). This peak is also associated with significant energy in the k = 2 terms and some (lower amplitude) energy in the k = 1 term of the HD, which suggests a contrast in anisotropy with nearly horizontal symmetry. The transverse component rose plot for this interface exhibits a similar pattern to the HD analysis and the HD modeled rose plot, with a relatively clear 4-lobe polarity flip, which supports a contrast in anisotropy with horizontal symmetry (Fig. 4b). The second interface, at $t = 2.2$–2.35 s, is mostly visible in the HD from the presence of significant energy in both the k = 1 and k = 2 terms (Fig. 5). It is associated with only a small negative pulse at 2.2 s in the k = 0 term. Based on the energy contained in the k = 1 and k = 2 terms, we infer a contrast in anisotropy across this interface, associated with either a dipping interface or a plunging axis of symmetry (Fig. 5). Interestingly, the zero-delay time energy on the transverse component RF exhibits a generally good fit with the opposite polarity observed on the transverse component at t = 2.2–2.35 s (Fig. 3a), as would be expected for an isotropic dipping interface; however, given the substantial k = 2 energy, a contrast in anisotropy is very likely to also be present. The direction analysis for this interface yields an estimate of a ~45°/225° for a tilt direction, an inference that is generally consistent with visual inspection of the transverse component rose diagram (Fig. 4b). This axis could either represent the dip of an isotropic interface or the plunge of an anisotropic symmetry axis.

The third interface beneath LPAZ shows high amplitude in the non-constant stack and is visible in the HD from the presence of significant energy in both the k = 1 and k = 2 terms at 3.2–3.5 s (Fig. 5). Both the HD and the rose plot (Fig. 4b) suggest that this peak is associated with

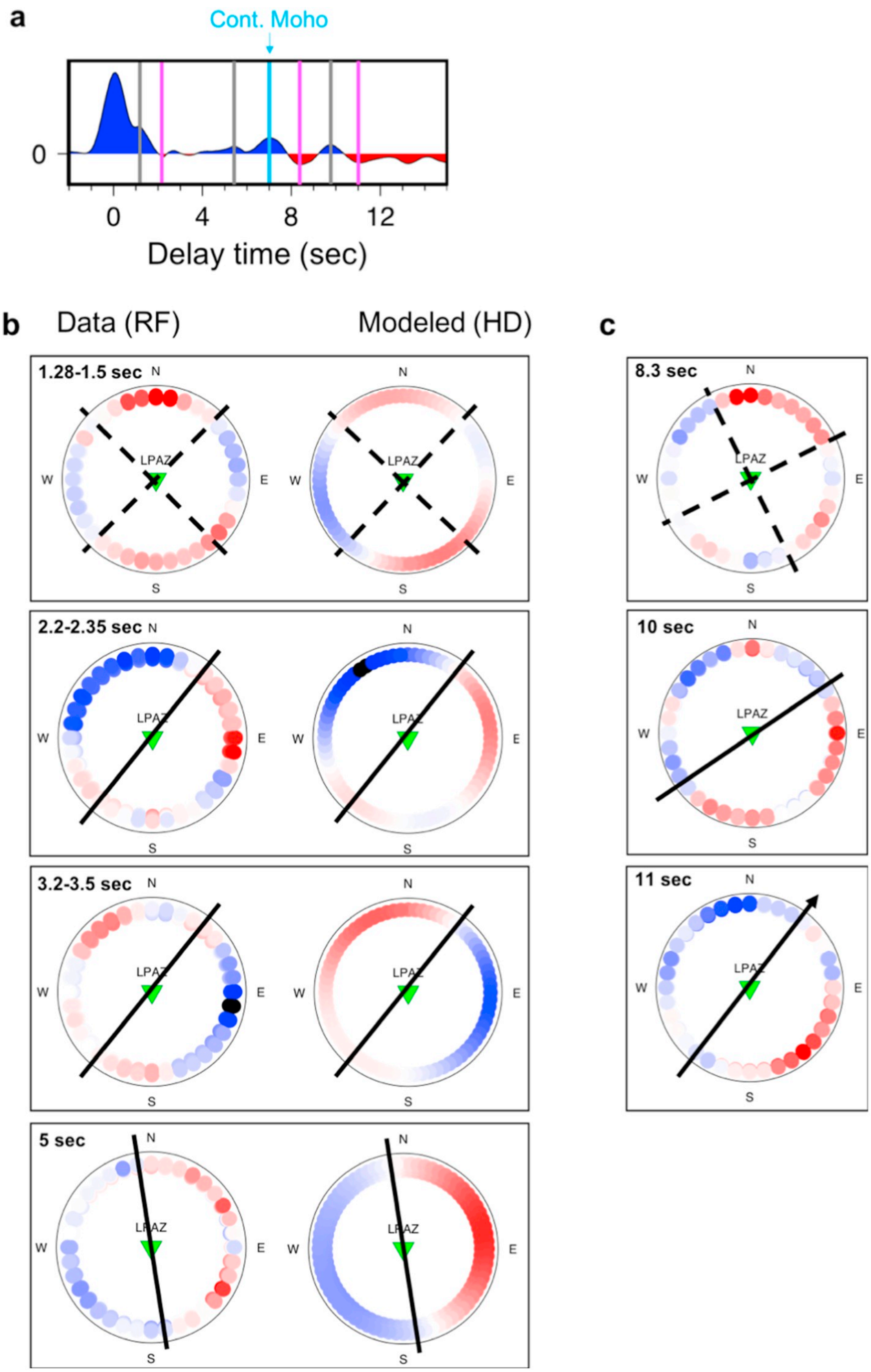

Fig. 4. Plots illustrating the characteristics of additional interfaces (other than the Moho) beneath LPAZ. (a) Single-station binned-stacked quasi-radial component RFs (same as Fig. 3c, but presented again here for easy comparison with later panels and to highlight interfaces other than the Moho), annotated with lines showing the Moho pick (cyan) and other major interfaces illustrated in (b); gray lines mark positive picks and magenta lines mark negative ones. (b) Rose plots showing the backazimuthal variability in amplitude of the transverse component RFs (left) and their associated modeled energy from the HD analysis (right) for the intracrustal interfaces marked in (a) (left of the Moho) and an additional interface (3.2–3.35 s) revealed only from the HD analysis. This panel presents examples of the comparison between the transverse component RF and the HD model, to illustrate the remarkably good fit between them. The delay time range associated with each interface is shown in the upper left corner. Solid black lines represent inferred tilt axis directions based on HD direction analysis; dashed black lines relate to changes in the orientations of anisotropy symmetry axes for the contrast in close to horizontal anisotropy. Note that the 90° ambiguity for the latter reflects the four polarity changes across the backazimuth in the transverse component RF. (c) Rose plots showing the backazimuthal variability in amplitude of the transverse component RFs for the lithospheric mantle interfaces marked in (a) (right of the Moho). The delay time associated with each interface is shown in the upper left corner as in (b). Plotting conventions are again as in the left row of (b), except the black arrow that represents inferred dip direction based on HD direction analysis. (For interpretation of the references to colour in this figure legend, the reader is referred to the web version of this article.)

either a mixture of a dipping interface with anisotropy or anisotropy with a plunging symmetry axis; our direction analysis suggests a tilt direction of ~30°/210°. The fourth and last intracrustal interface has a relatively smaller amplitude (but above our cutoff) positive arrival at 5–5.4 s visible in the single-station stack (Fig. 4a) and in the k = 0 term of the HD (Fig. 5). Both the HD and the rose plot (Fig. 4b) suggest that this peak is associated with either a mixture of a dipping interface with anisotropy or anisotropy with a plunging symmetry axis; our direction analysis suggests a tilt of ~170°/350° (Fig. 4b). Taken together, the presence of multiple interfaces within the crust beneath LPAZ that include a contrast in anisotropy suggests the presence of complex anisotropic layering.

Below the Moho, we identify three additional interfaces within the lithospheric mantle. A significant negative arrival at 8.3 s, visible in the single-station stack (Fig. 4a) and the k = 0 term of the HD (Fig. 5), may correspond to a mid-lithospheric discontinuity (MLD) phase. The HD analysis combined with the rose plots (Fig. 4c) suggests that the 8.3 s interface is associated with some contrast in anisotropy, which is consistent with observations elsewhere of a contrast in anisotropy across a velocity discontinuity within the mantle lithosphere (e.g., Ford et al., 2016; Wirth and Long, 2014). Next, we see an interface with an anisotropic contrast that is visible in the HD from the presence of significant energy in the k = 1 and k = 2 terms at 9.75–10 s (Figs. 5) and is associated with a small positive pulse at 9.75 s in the single-station

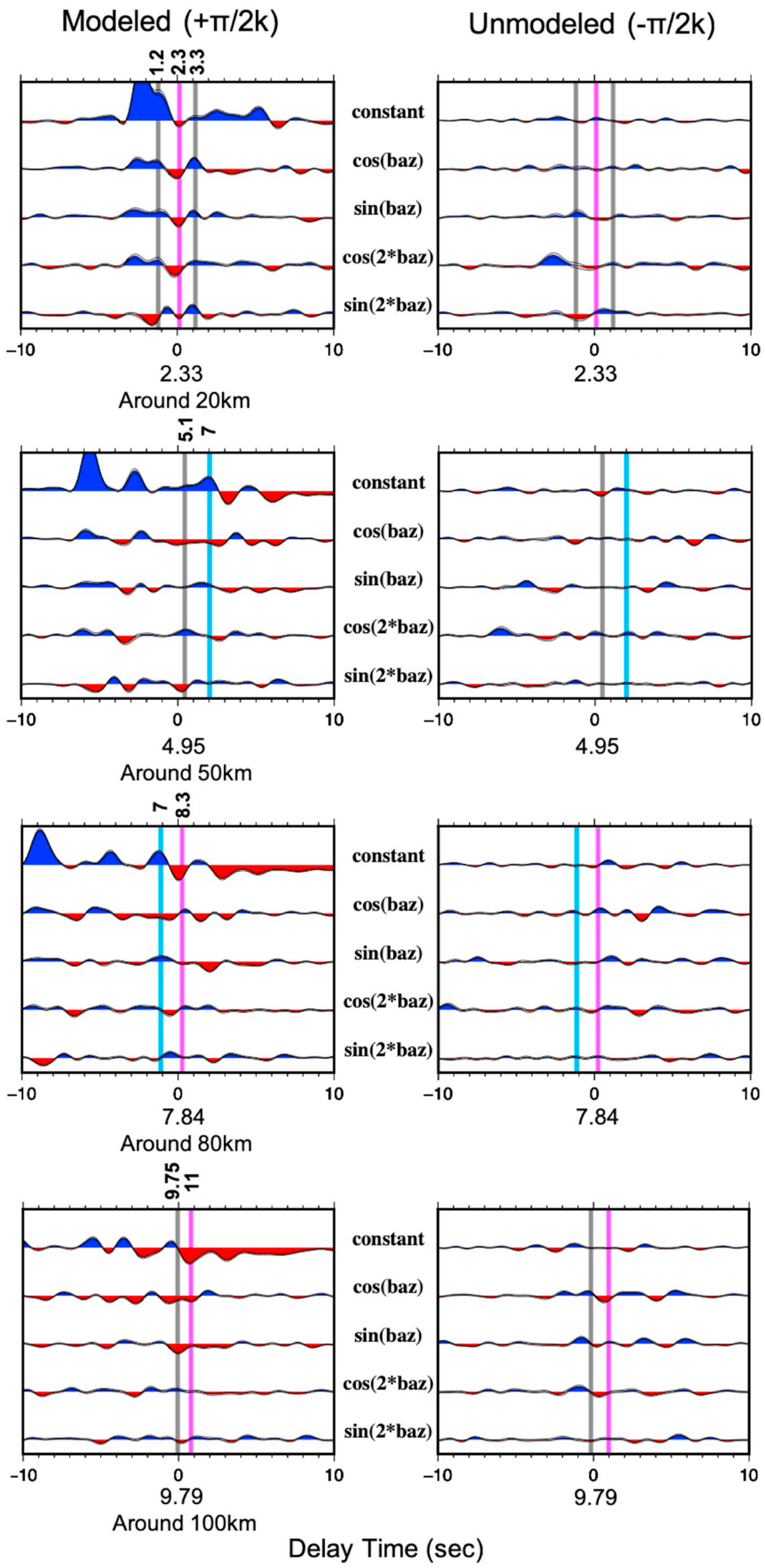

Fig. 5. Harmonic decomposition results beneath LPAZ, computed around different target depths (see labels beneath each plot on the left) corresponding to the additional interfaces (other than the Moho, see Fig. 4), and their minimum and maximum bootstrap error estimates (because of the small error estimates, these are nearly indistinguishable from the main traces). Left panels show the modeled ($+\pi/2\,k$) portion of the HD on the left, with the top trace corresponding to the k = 0 (constant) term, the next two traces corresponding to the k = 1 terms, and the final two traces corresponding to the k = 2 terms. The right panels show the unmodeled or suppressed ($-\pi/2\,k$) portion of the HD. Beneath each time axis, we show the center time associated with the target depth (in sec) beneath the t = 0 reference time. The cyan line marks the Moho, gray lines mark positive picks and magenta lines mark negative ones (near a delay time of zero sec on the x axis; here a zero sec delay time corresponds to the expected arrival time for a conversion at the target depth). Delay times relative to the direct P arrival are labeled above each interface line. (For interpretation of the references to colour in this figure legend, the reader is referred to the web version of this article.)

stack (Fig. 4a). The direction analysis suggests a plunging axis of symmetry around ~70°/250°, reasonably consistent with the rose plot diagram (Fig. 4c). Lastly, a deeper negative arrival at 11 s, visible in the single-station stack (Fig. 4a) and the k = 0 term of the HD (Fig. 5), may also correspond to a mid-lithospheric discontinuity (MLD) or, alternatively, to the velocity drop at the lithosphere-asthenosphere boundary (LAB). This interface appears to be dipping, with a dip direction of ~33°. The zero-time energy exhibits a polarity that fits well with the predictions from the transverse component RF energy for this 11 s interface. This inference may agree with the notion that the 11 s interface relates to the LAB; furthermore, it may be consistent with evidence from seismic tomography for the presence of a fast velocity anomaly thought to correspond to (possibly delaminating) lithosphere beneath LPAZ and the surrounding region (Ward et al., 2016). We emphasize, however, that converted waves at delay times of ~10 s or greater may be difficult to resolve precisely with our method, due to the characteristics of the multitaper correlation RF estimator (Park and Levin, 2000; also see discussion in Ford et al., 2016), so the interpretation of deeper interfaces must be done with some caution.

4.2. CAUGHT stations in Bolivia

The temporary CAUGHT deployment of broadband seismometers operated between 2010 and 2012 in southern Peru and northern Bolivia (Fig. 1). We computed quasi-radial and transverse component RFs as a function of backazimuth (Fig. S3) and single-station binned quasi-radial component RF stacks for a subset of 17 CAUGHT stations deployed in a dense, roughly trench-perpendicular line (SW-NE transect) surrounding LPAZ station. Additionally, we computed HD analysis for these CAUGHT stations with a target depth appropriate for examining the Moho interface (Fig. S4). Subsequently, we also computed HD analysis for a subset of these stations targeting a midcrustal feature visible in the single-station stacks, as described below. Because of the relatively short deployment time, the backazimuthal coverage we achieved in our analysis was substantially poorer than what we obtained for LPAZ (see Fig. 1b for an example at CAUGHT station CB28). Our analysis and interpretation strategy, therefore, focuses on whether we can identify some of the same interfaces (e.g., the Moho) beneath the CAUGHT stations as beneath LPAZ, and whether the inferred dipping and/or anisotropic characteristics of these interfaces are consistent or laterally variable across the transect.

At 9 out of the 17 CAUGHT stations we analyzed, the single-station stacks show a clear, strong, positive pulse that varies between 5 and 8.5 s after the P arrival, which we interpret as the positive isotropic velocity change across the Moho. Beneath LPAZ, the Moho is associated with some combination of a dipping interface with a contrast in anisotropy, and/or the presence of anisotropy with a plunging symmetry axis either directly above or directly beneath the Moho (as discussed in Section 4.1). In order to evaluate whether this pattern is consistently found across the CAUGHT dense line, we computed HDs surrounding the interpreted Moho depth for the subset of 9 CAUGHT stations that have clear Moho arrivals on the single-station stacks. Similar to our analysis for LPAZ, we stacked the non-constant terms of the HD analysis together to identify interfaces with a likely anisotropic component. This analysis reveals high amplitude in the k = 1 and k = 2 terms associated with the Moho interface for all 9 stations, suggesting that the contrast of anisotropy across the Moho is a robust feature that extends laterally along the CAUGHT line (Fig. S4). Our direction analysis shows changing symmetry axis orientations for the contrast in anisotropy across these interfaces, ranging from ~45°/225° to ~150°/330° (Fig. 6a). Based on the HD direction analysis, it seems clear that there is lateral variability in the geometry of the anisotropy in the deep crust just above the Moho, in the uppermost mantle just beneath it, or both. This, in turn, suggests lateral variability in the deformation geometry in the deep crust and/or uppermost lithospheric mantle along the CAUGHT array.

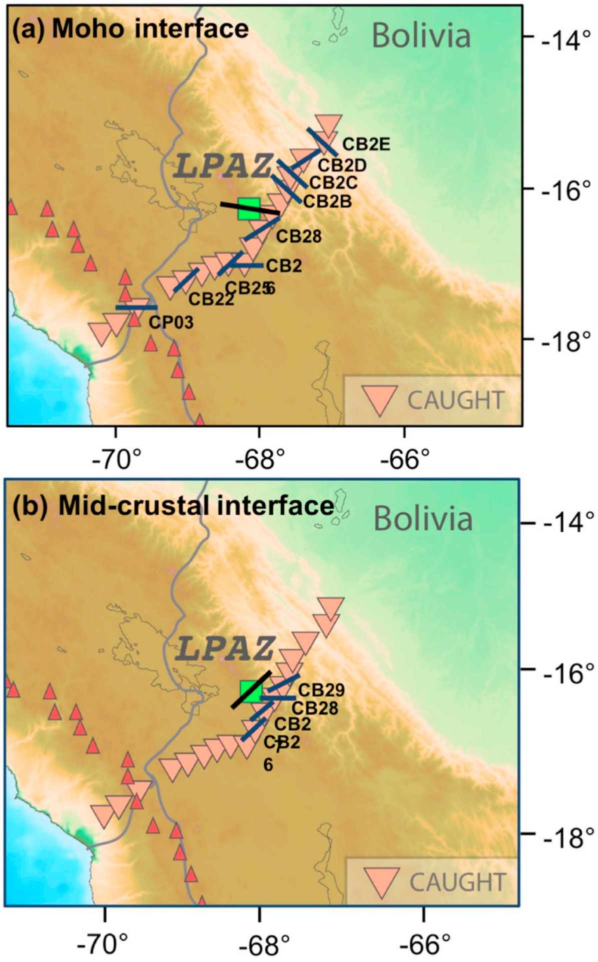

Fig. 6. Summary map of the properties of two major interfaces as derived from the HD analysis beneath LPAZ and CAUGHT temporary stations. The map shows location of CAUGHT stations (orange triangles) along with LPAZ; background colors show topography. (a) We show results for 9 out of the 17 CAUGHT stations we analyzed; these stations showed a clear Moho interface and their direction analysis reveal changing tilt axis directions along CAUGHT dense line. (b) Same as (a), but here we focus on an intracrustal interface that is visible at LPAZ and at four of the CAUGHT stations we analyzed. The black lines represent inferred tilt axis directions based on HD direction analysis.

In addition to the Moho interface, we also examined the CAUGHT RF gathers and the single-station stacks to look for evidence of other interfaces with persistent features along the array that may shed light on the anisotropic structure. Again, the relatively poor backazimuthal coverage precludes a detailed analysis. However, one notable observation is the presence of consistent mid-crustal feature, with a negative arrival around 2–3 s, at four of the CAUGHT stations located just to the south of LPAZ (CB26 through CB29). We computed the HD surrounding these target depths for these four stations (Fig. 6b); this analysis reveals general similarity (at 3 out of the 4 stations) between its anisotropic characteristics and tilt directions (between ~40°/220° to ~55°/235°) and the pattern at LPAZ. This observation suggests that the anisotropic mid-crustal feature we infer beneath LPAZ may extend roughly 100 km to the south in a similar geometry.

4.3. Station NNA, Peru

Station NNA (Fig. 1) is deployed close to the coast, west of the Western Cordillera, north of the subducted Nazca Ridge, and within the Peru flat slab segment. Previous detailed analyses of shear wave splitting behavior beneath NNA (Eakin and Long, 2013; Eakin et al., 2014,

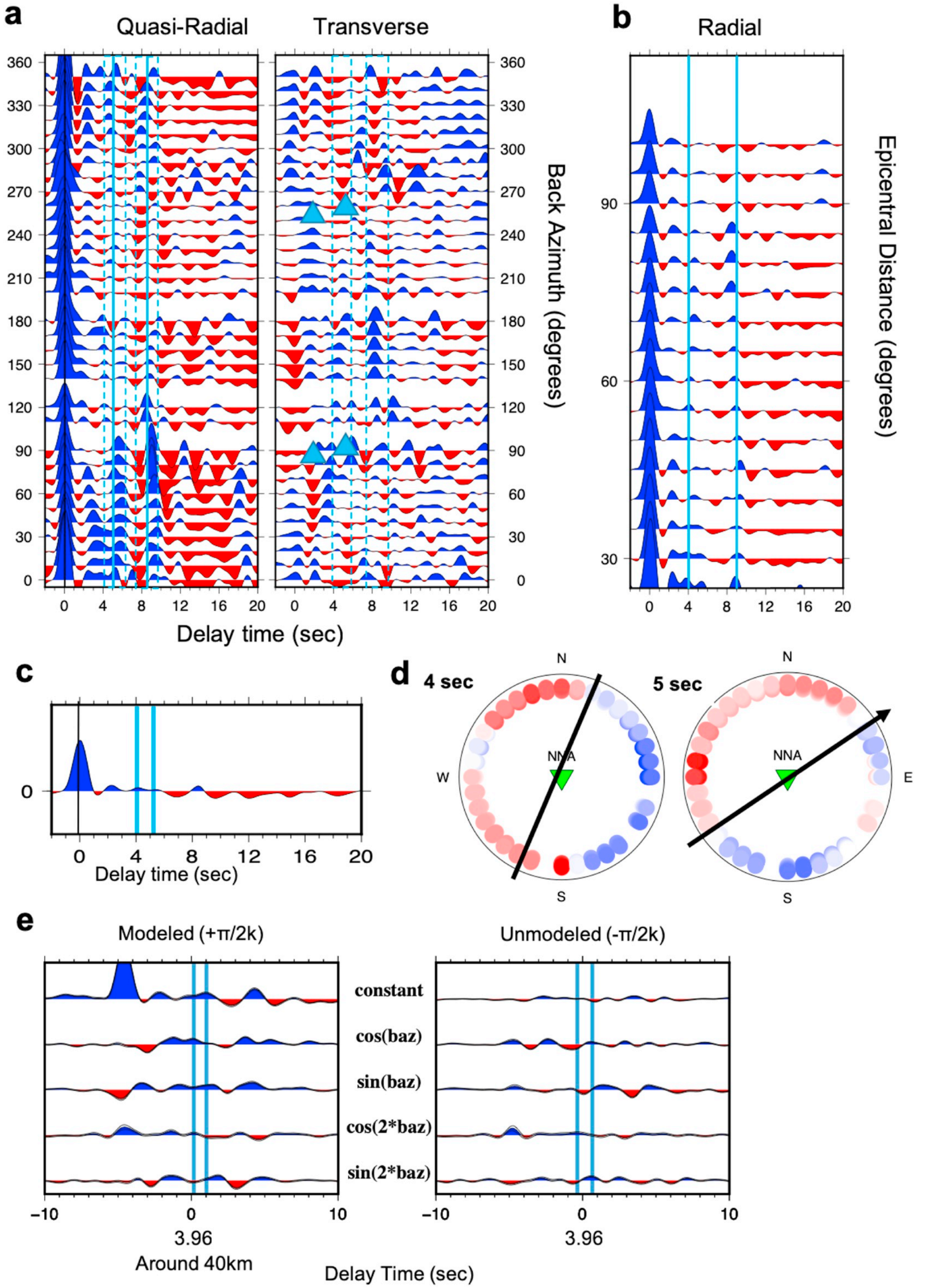

Fig. 7. Results of our RF analysis at station NNA, with an emphasis on characterizing the overriding plate Moho arrival. (a) Quasi-radial (left) and transverse (right) component RFs, that have been migrated, gathered in backazimuthal bins (as indicated on y axis), and stacked. Plotting conventions are as in Fig. 3, except that here there are two Moho time ranges indicated, with the earlier one corresponding to the overriding plate Moho and the later one corresponding to the slab Moho. Triangles on transverse component RFs mark the 2-lobe polarity changes associated with each Moho, as in Fig. 3. (b) Stacked quasi-radial component RFs, gathered as a function of epicentral distance (as indicated on y axis). As in (a), the cyan lines mark the overriding plate and slab Moho picks. (c) Binned-stack of the quasi-radial component RFs over all backazimuths and epicentral distances. The cyan lines mark the two options inferred for the continental Moho (see Section 4.3). (d) Rose plot of the transverse component RF amplitude over the two time ranges corresponding to the inferred continental Moho (black line marks the anisotropy tilt axis of symmetry and the black arrow marks an interface dip direction, both based on HD direction analysis). (e) Harmonic decomposition results, computed around a target depth (~40 km) corresponding to the options inferred for the continental Moho. Plotting conventions are again as in Fig. 3. (For interpretation of the references to colour in this figure legend, the reader is referred to the web version of this article.)

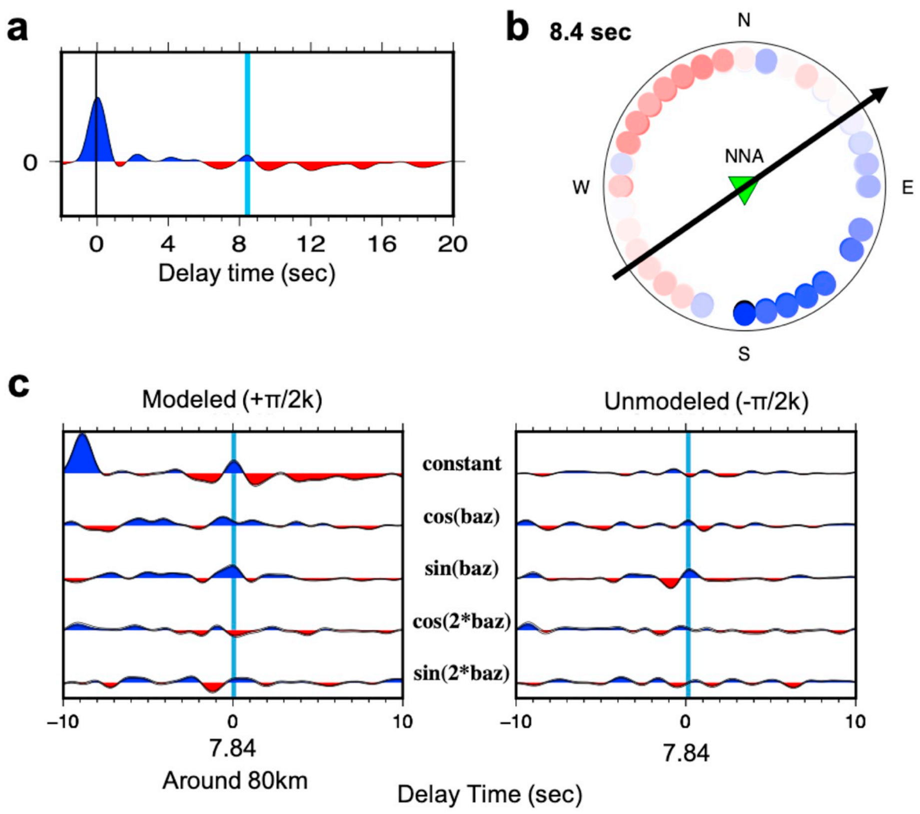

Fig. 8. Results of our RF analysis at station NNA characterizing the oceanic slab Moho arrival. (a) Binned-stack of all quasi-radial component RFs, over all backazimuths and epicentral distances. The cyan line marks the slab Moho. (b) Rose plot of the transverse component RF amplitude over the time range corresponding to the slab Moho pick (black arrows mark the dip direction based on HD direction analysis). (e) Harmonic decomposition results, computed around a target depth (~80 km) corresponding to the oceanic slab Moho. Plotting conventions are the same as corresponding diagrams in Fig. 3. (For interpretation of the references to colour in this figure legend, the reader is referred to the web version of this article.)

2015), as well as models for azimuthal anisotropy based on surface waves (Antonijevic et al., 2016), revealed evidence for multiple layers of anisotropy beneath this region. This inference can be further tested with RF observations, which combine the advantages of good lateral resolution as well as the ability to provide specific depth constraints on sharp anisotropic interfaces. Figs. 7 and 8 show the results of our RF analysis beneath NNA, following the same plotting conventions described in Section 4.1 for LPAZ.

The quasi-radial component RFs beneath NNA (Fig. 7a) are complex, exhibiting two or three positive pulses between 2 and 6 s. Strikingly, there is a great deal of backazimuthal variability in the quasi-radial RF characteristics at these delay times, with some arrivals clearly visible within certain backazimuthal ranges and completely absent in others. This observation suggests that some aspects of the RFs may reflect heterogeneous structure (that is, out-of-plane with respect to the PULSE dense line). Because of the complexity of the observations, it is unclear which one of these pulses is associated with the Moho of the overriding plate, although the later peaks (around 4 and 5 s) fit better with previous interpretations of radial component RFs that included common conversion point (CCP) stacking (Bishop et al., 2017). The single-station quasi-radial RF stack (Fig. 7c) illustrates a clear positive peak at 4 s; on the other hand, the HD displays a clear positive peak at 5 s (Fig. 7e) (The difference between the single-station stack and the HD may relate to the different target depth in the HD migration). Our preferred interpretation is that the 5 s peak represents the positive isotropic velocity change across the continental Moho, corresponding to an approximate depth of 50 km (based on the AK135 velocity model). We further interpret the striking azimuthal patterns in the timing and amplitude associated with this arrival as reflecting a dipping Moho interface, which is also inferred from CCP stacked images presented in Bishop et al. (2017). The transverse component RFs (Fig. 7a), along with the rose plots (Fig. 7d), both illustrate a two-lobed polarity change around this time interval of the Moho, also suggesting a dipping interface. Furthermore, the zero-delay time on the transverse component RF exhibits a reasonable fit to the opposite polarity expected for an isotropic dipping interface. The HD model displays a larger amplitude in the sin(ϕ) term for the 5 s interface, with little to no energy in the k = 2 term. The direction analysis suggests an estimated dip direction of ~70–80°; this direction is close to the convergence direction between the Nazca and South American plates (e.g., Kreemer et al., 2014). Near the 4 s time interval, the HD mostly exhibits energy in the cos(ϕ) term, with smaller amplitudes in the k = 2 terms; taken together, this suggests an anisotropy contrast just above the dipping Moho interface. The direction analysis suggests an estimated tilt direction of ~30°/210°. The observation of multiple interfaces near the base of the crust, with significant azimuthal variability in the character of both quasi-radial and transverse component RFs, suggest the presence of multiple anisotropic layers with complex geometries in the deep crust of the overriding plate.

A clear positive pulse between 7.5 and 9.5 s after the P arrival, with a peak at 8.4 s, is also evident in both the quasi-radial component RFs (Fig. 7a) and the single-station stack (Figs. 8a) (the peak itself is visible most clearly in the single-station stack). We interpret this peak as the positive isotropic velocity change across the dipping slab oceanic Moho, again consistent with the interpretation of the stacked CCP images in Bishop et al. (2017). This time interval corresponds to ~80–85 km depth based on the AK135 velocity model. Both the transverse component RFs and the rose plot (Fig. 8b) show a clear 2-lobed pattern at this time interval, suggesting a dipping interface of the crust-mantle transition in the subducting slab, as expected from previous explorations of the slab geometry here (e.g., Antonijevic et al., 2015; Bishop et al., 2017; Kumar et al., 2016). This inference is further supported by the zero-delay time arrivals on the transverse component RF that exhibit the opposite polarity expected for an isotropic dipping interface (Fig. 7a). Moreover, the HD (Fig. 8c) also shows a positive amplitude in the constant term at the time interval associated with the oceanic Moho interface, along with a positive k = 1 pulse mostly in the sin(ϕ) term (with a much lower amplitude in the cos(ϕ) term), strengthening the dipping interface inference. Our direction estimate from the HD analysis suggests that the interface associated with the subducting slab

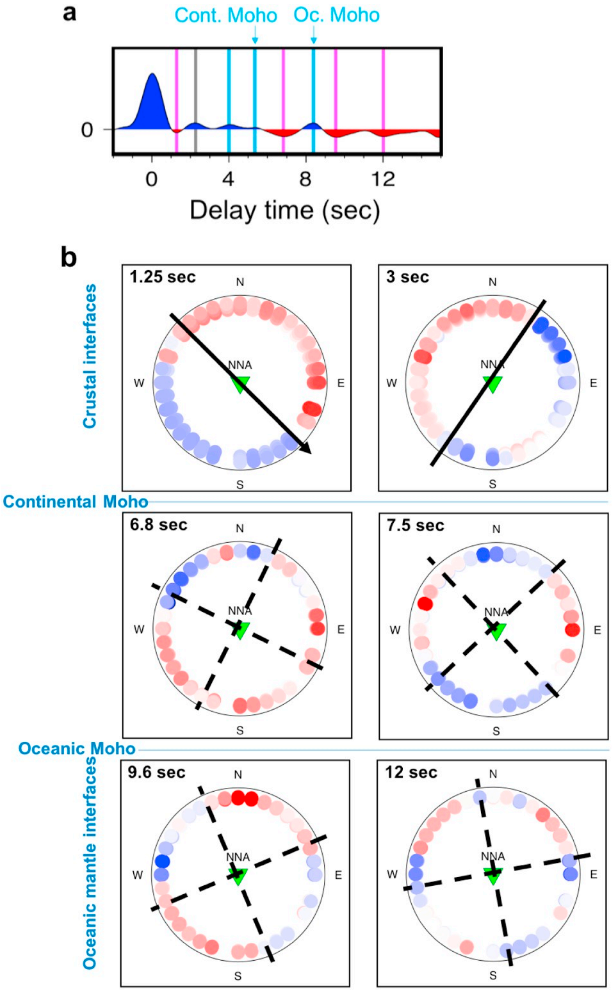

Fig. 9. Plots illustrating the characteristics of additional interfaces (other than the continental and slab Mohos) beneath NNA. (a) Single-station binned-stacked quasi-radial component RFs (same as Fig. 7c), annotated with lines showing the Mohos picks (cyan) and other major interfaces illustrated in (b); gray lines mark positive picks and magenta lines mark negative ones. (b) Rose plots showing the backazimuthal variability in amplitude of the transverse component RFs for interfaces marked in (a) other than the overriding plate and slab Mohos, including an additional interface (3 s) revealed only from the HD analysis. They are arranged by depth, such that interfaces within the overriding plate crust are shown in the top row, interfaces between the overriding plate and the slab Moho are shown in the middle row, and interfaces beneath the subducting oceanic crust are shown in the bottom row. The delay time associated with each interface is shown in the upper left corner. Black lines represent inferred tilt axis or dip (arrow) directions based on HD direction analysis; dashed black lines relate to changes in the orientations of anisotropy symmetry axes for the contrast in close to horizontal anisotropy. (For interpretation of the references to colour in this figure legend, the reader is referred to the web version of this article.)

Moho has an estimated dip direction of ~65–70°, agreeing well with the rose plot diagram and also generally consistent with previous results (Bishop et al., 2017). Interestingly, the k = 2 terms in the HD model show only very small amplitudes in this time range, suggesting that a contrast in anisotropy across the slab Moho (that is, a contrast between the oceanic crust of the slab and its underlying mantle lithosphere) is not required by the data.

In addition to the prominent pulses associated with the inferred continental Moho and oceanic slab Moho, we also see evidence for additional interfaces represented by positive and negative pulses seen in the single-station stack (Fig. 9a) and in the k = 0 term of the HD (Fig. 10), as well as high energy peaks in the stacked non-constant terms. The mid-crustal features include three interfaces, starting with a small negative pulse at 1.25–1.8 s after the P arrival that is visible in the single-station stack (Fig. 9a) and k = 0 term of the HD (Fig. 10). This arrival is also associated with significant energy in the k = 1 terms. The HD analysis and rose plot (Fig. 9b) at 1.25–1.8 s delay time fit well with a dipping interface with a dip direction of ~150–160°, with no need to invoke an anisotropy contrast. The zero-delay time energy on the transverse component RF for this 1.25–1.8 s interface does not exhibit the opposite polarity expected for an isotropic dipping interface; however, it is clear that there are multiple dipping interfaces (including both Mohos) beneath NNA, and any zero-time energy from these interfaces likely undergoes interference. The second intracrustal interface is an isotopic velocity change visible as a positive arrival at 2.2 s in the single-station stack and the k = 0 HD term (Figs. 9a, 10). This interface is not associated with a clear anisotropic signal; while a mix of two-lobe and four-lobe polarity changes may be present, the patterns are not particularly clear, and there is a fairly substantial component of the RF signal that is unmodeled by the HD expansion (Fig. 10). The last intracrustal interface (at t = 3–3.3 s) shows high energy in the stack of the non-constant terms, and is associated with significant energy in both the k = 1 and k = 2 terms (Fig. 10). Both the HD and the rose plot (9b) suggest that this peak is associated with either a mixture of a dipping interface with anisotropy or anisotropy with a plunging symmetry axis; our direction analysis suggests a tilt direction of ~34°/214°.

A clear, strong negative pulse is apparent on the quasi-radial component RFs (Fig. 7a) between the two inferred Moho arrivals (that is, the overriding plate Moho and the subducting slab Moho), which suggests a drop in velocity within the mantle wedge. In the backazimuthal gather, the peak of this negative pulse moves between 6.5 and 7.5 s, whereas the single-station stack shows a clear peak at 6.8 s (Fig. 9a). Our HD analysis reveals a moderate anisotropic signal with more energy in the k = 2 terms, suggesting a horizontal anisotropic contrast with symmetry axes oriented at ~35°/135° (Fig. 10). An inspection of the rose plots reveals a mix of two-lobe and four-lobe polarity changes (Fig. 9b). A second (perhaps related) interface at t = 7.5 s is revealed only by the presence of significant energy in both the k = 1 and k = 2 terms in the HD (Fig. 10). The HD suggests that this peak may be associated with anisotropy with a plunging symmetry axis, whereas the rose plot show a clear 4-lobe pattern (Fig. 9b); our direction analysis suggests a tilt azimuth of ~50°/230°.

Lastly, we see two more negative arrivals after the arrival from the oceanic slab Moho; these arrive at delay times of 9.6 and 12 s after the direct P arrival. It is likely that one of these corresponds to the velocity drop across the base of the subducting slab, but at these relatively large delay times associated with these interfaces, caution must be exercised in their interpretation. Each of these arrivals seems to have a component of anisotropy associated with them, visible in the rose plots and HD (Figs. 9b, 10). Direction analysis for the interface at 9.6 s suggests a tilt of ~145°/325°; at t = 12 s, the azimuthal pattern is too complicated to extract a robust direction estimate.

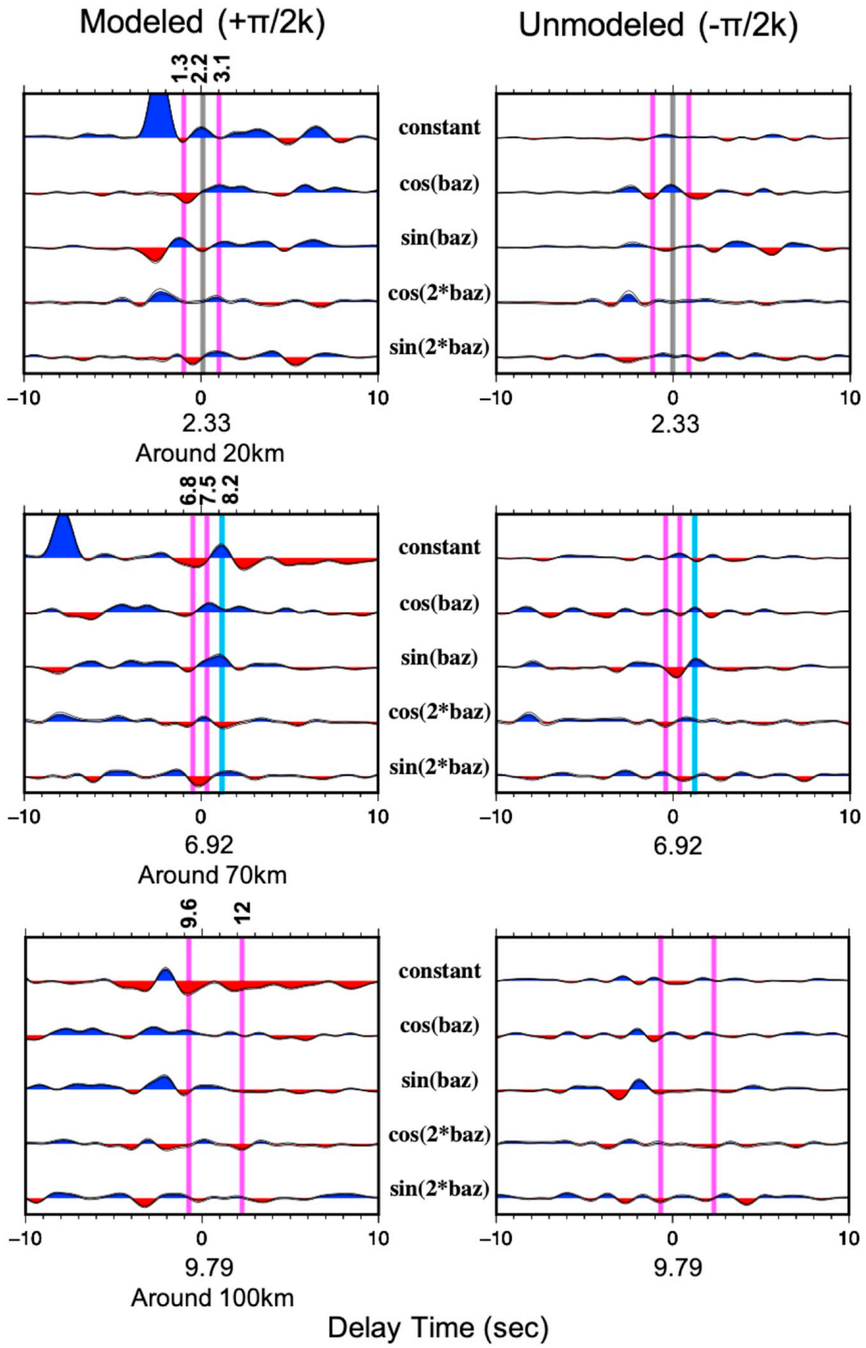

Fig. 10. Harmonic decomposition results beneath NNA, computed around different target depths (see labels beneath each plot on the left) corresponding to the additional interfaces (other than the Moho, see Fig. 9), and their minimum and maximum bootstraps. Plotting conventions are as in Fig. 5, except that here the cyan lines mark both options for either the overriding plate Moho (HD of 20 km target depth) or the subducting slab Moho (HD of 70 and 100 km target depth). Delay times relative to the direct P arrival are labeled above each interface line. (For interpretation of the references to colour in this figure legend, the reader is referred to the web version of this article.)

4.4. PULSE stations in Peru

The temporary PULSE deployment consisted of 40 broadband seismometers, which operated between 2010 and 2013 in southern Peru. We computed RFs (Fig. S5) and single-station quasi-radial RF stacks, along with HD analysis, for a subset of 11 of these stations (Fig. 1) that made up a dense linear transect stretching from station NNA outside Lima to the northeast across the Andes. As with the CAUGHT data, the relatively short deployment times mean that the azimuthal coverage is poorer than at permanent station NNA, but we investigated whether major interfaces beneath NNA seem to persist across the PULSE dense line, and whether their anisotropic characteristics change across the transect. Unfortunately, the azimuthal coverage for PULSE stations is generally even poorer than for CAUGHT stations, due to the global distribution of seismicity in our epicentral distance range of interest (Fig. 2, S5).

This generally poor azimuthal coverage, and the complex character of the interfaces inferred beneath permanent station NNA, made it difficult to identify interfaces whose anisotropic and/or dipping characteristics could be tracked across the dense PULSE array. The exception to this was the subducting slab Moho, which is visible on the quasi-radial RFs at NNA, with a clear dipping component, and which we were able to trace across a portion of the PULSE transect. Specifically, for 6 out of the 11 PULSE stations we analyzed, both the single-station stacks and the k = 0 term of the HD (Fig. S6) show a clear positive pulse between 8 and 10 s after the P arrival, which we interpret as being due to the oceanic slab Moho. Interestingly, the corresponding transverse component and our direction analysis based on the HD (Fig. 11) for these PULSE stations show similar characteristics and dip directions (between 50° to 80°) as those for NNA. This may suggest that the slab Moho dips to the northeast beneath these stations; on the other hand, the HD model of the PULSE stations shows some energy in the k = 2

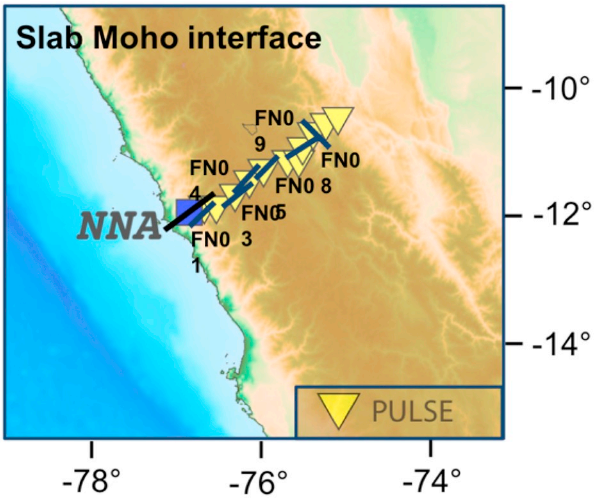

Fig. 11. Summary map of the properties of the slab Moho interface beneath NNA and selected PULSE temporary stations as derived from the HD analysis beneath. The map shows location of PULSE stations (yellow triangles) along with NNA; background colors show topography. The black lines represent inferred tilt axis directions based on HD direction analysis. (For interpretation of the references to colour in this figure legend, the reader is referred to the web version of this article.)

terms (in contrast to NNA), perhaps indicating some contrast in anisotropy (Fig. S6).

5. Discussion

5.1. Complex crust and upper mantle anisotropy beneath Peru and Bolivia

Our analysis of structure beneath both LPAZ and NNA focused on identifying peaks of energy visible on the single-station stack, as well as considering the constant and non-constant terms in the HD model (following Ford et al., 2016). The latter approach helps to identify interfaces with isotropic contrast in velocity, along with dipping and anisotropic interfaces, in a more straightforward way than visual inspection. For both LPAZ and NNA, most of the peaks inferred from the non-constant HD terms corresponded to peaks in the constant term (and/or in the single-station stack), which suggests that the interfaces we identified mostly represent co-located isotropic and anisotropic contrasts. Beneath both stations, we see evidence for multiple dipping and anisotropic interfaces, including layered anisotropy within the crust, particularly at station LPAZ. Although the temporary station data are sparse, they do express a few of the features inferred beneath the long-running stations. A simplified cartoon diagram of the layered structure in the crust and upper mantle that we infer from our analysis beneath southern Peru and northern Bolivia is shown in Fig. 12. In general, our results highlight the remarkable complexity of the crust and upper mantle structure beneath the subduction zone in South America, as discussed in further detail below.

5.2. Comparison with previous results: RF studies

Beneath LPAZ, we observed and described the continental Moho and seven additional interfaces (Fig. 12a). Our inferences can be compared with results from a previous study by Ryan et al. (2016), who calculated RFs to investigate crustal thickness beneath the Central Andean Plateau using data from CAUGHT and LPAZ. Their results show the continental Moho beneath the CAUGHT transect as an interface whose depth varies from ~40 km to nearly ~80 km, with an approximate depth of ~60–70 km beneath LPAZ. These depths are consistent with our estimates. The two-dimensional CCP stack of Ryan et al. (2016) along the CAUGHT dense line (their Fig. 5) suggests that the Moho dips gently to the SW. Our orientation calculation for LPAZ estimated a tilt azimuth to the ESE-WNW. The contrast between this direction and the dip direction inferred by Ryan et al. (2016) may strengthen the inference from the rose plot together with the HD direction analysis that the k = 1 terms reflect a plunging axis of anisotropy, rather than an isotropic interface dip direction. Furthermore, our CAUGHT single-station RF stacks reveal a shallower Moho to the NE of LPAZ (in agreement with Ryan et al., 2016), and our HD analysis suggests that this Moho interface is associated with a contrast in anisotropy. Our direction analysis shows changing axis of tilt for the contrast in anisotropy across the CAUGHT line, implying a lateral variation in the geometry of anisotropy in either the lowermost crust, the uppermost mantle, or both. Therefore, we interpret the LPAZ Moho as involving a plunging axis of anisotropy whose geometry changes laterally along the CAUGHT dense line. This adds important insight into the spatial variation in anisotropy that goes beyond previous insights into Moho geometry gleaned from the CCP stack of Ryan et al. (2016).

In addition to the Moho, Ryan et al. (2016) observed a complex layered structure within the crust beneath the CAUGHT dense line (their Fig. 5). They note two major upper crustal interfaces: a shallower one associated with a prominent positive arrival, and a deeper one associated with a negative arrival. They suggested the positive arrival corresponds to the top of basement rocks below a basal fault at approximately ~10 km depth. The negative arrival was interpreted by Ryan et al. (2016) as the top of a low velocity zone (LVZ) starting at ~20 km depth; this feature is most strongly visible beneath the Eastern Cordillera, but is also visible beneath LPAZ. These two interfaces may correspond to our positive and negative arrivals at 1.2–1.5 s and 2.2 s beneath LPAZ. If this is correct, then our analysis suggests that each of these interfaces may be associated with a strong contrast in seismic anisotropy, in addition to an isotropic velocity contrast. Additionally, our CAUGHT dense array analysis identifies a crustal anisotropic feature, associated also with a negative arrival on the single-station quasi-radial stack, at around 2–3 s that seems to have a similar anisotropic signal as the 2.2 s LPAZ interface (Fig. 6b). We suggest that this anisotropic mid-crustal feature may extend NE-SW for roughly 100 km surrounding LPAZ in a similar geometry, a wider extent than identified by Ryan et al. (2016).

Beneath NNA, we observed and described the continental Moho, the oceanic subducting Moho, and eight additional interfaces (Fig. 10b). A recent study by Bishop et al. (2017) applied a similar methodology as Ryan et al. (2016) to the computation and stacking of RFs beneath southern Peru, using data from PULSE and NNA. Their analysis clearly reveals the continental Moho beneath PULSE dense transect (their Fig. 3, see cross-section C-C′) at a depth of ~40 km near the coast to ~60 km depth beneath the Eastern and Western Cordilleras. The CCP image of Bishop et al. (2017) suggests a continental Moho beneath NNA that dips to east and is at a depth of ~40–45 km depth, consistent with our findings (Fig. 7). Bishop et al. (2017) also indicate that the continental Moho arrival beneath the forearc is diffuse and low-amplitude, suggesting a complex or gradational interface. This suggestion is consistent with our observation of complicated RFs with multiple peaks whose amplitude vary substantially with backazimuth, as well as the likely presence of anisotropy (Figs. 7, 12b). Furthermore, Bishop et al. (2017) estimated that the Nazca plate's subducting oceanic Moho lies around 80 km depth beneath NNA and that the distance between the continental Moho and the oceanic Moho is around 40 km at this region. These interpretations are consistent with our results (Figs. 7-8).

In addition to the Moho arrivals, Bishop et al. (2017) also observed complex intracrustal structure above the continental Moho, as well as an inferred velocity drop (corresponding to a negative arrival) between the base of the continental crust and the subducting slab. The intracrustal complexity beneath the PULSE line documented by Bishop et al. (2017) also finds expression in our analysis, including our inference of a shallow crustal interface (at ~1.2 s) with a dip that is apparently unrelated to the slab dip or convergence direction, a positive phase at 2.2 s that may include a component of anisotropy, as well as a clear anisotropic interface at ~3 s. The apparently complicated morphology of these interfaces, and their anisotropic nature, may indicate complex crustal deformation. The deeper negative arrival that we observe (between the continental Moho and the slab) may correspond to the top of a slow velocity layer described by Dougherty and Clayton (2014); Bishop et al. (2017) also documented a negative arrival that seems to be associated with this layer. Finally, the late converted phases that we document at 9.6 and 12 s may be related to structure beneath the subducting slab; specifically, Scire et al. (2016) documented slow velocity anomalies just beneath the flat slab in our study region.

5.3. Comparison with previous results: seismic anisotropy

A recent shear wave splitting study by Long et al. (2016) yielded evidence for significant anisotropy within and beneath the subducting oceanic Nazca plate beneath LPAZ and the CAUGHT array, along with somewhat weaker anisotropy in the mantle wedge and overriding plate above the slab. While shear wave splitting observations lack precise depth resolution, the interpretation of Long et al. (2016) is that much of the SKS splitting signal may be due to relatively deep upper mantle anisotropy, to which our RF analysis is not sensitive. The significant scatter in local S splitting measurements documented by Long et al. (2016) indicates significant heterogeneity in the anisotropic structure of the mantle wedge and/or the overriding plate, consistent with our inferences of multiple layers of anisotropy in the crust and upper mantle. A comparison between their local S splitting map around LPAZ and the anisotropic symmetries related to our ~5.4 and ~8.3 s interfaces (linked to the continental crust and the mantle wedge, respectively), show some similarities, with nearly trench-parallel directions dominating (Fig. 7 in Long et al., 2016). As discussed in Section 3, the k = 2 term contains azimuthal phase information on the orientation of azimuthal anisotropy symmetry axis. In the presence of a single anisotropic layer next to an isotropic layer, these orientations can be easily compared to the splitting data, but for a multi-layered anisotropic structure the comparison is less straightforward (Ford et al., 2016; Long et al., 2017).

Beneath the Peru flat slab segment, seismic anisotropy of the crust and upper mantle has been investigated through studies of shear wave splitting (Eakin and Long, 2013; Eakin et al., 2014, 2015) and surface wave tomography (Antonijevic et al., 2016). These studies all point to the presence of complex, multi-layered anisotropy; however, they lack depth resolution (in the case of shear wave splitting) or have relatively coarse lateral resolution (in the case of surface wave-based models). Our RF results provide complementary constraints to previous work on seismic anisotropy beneath Peru, and in particular do a much better job of characterizing anisotropy within the crust of the overriding plate than other methods.

Eakin and Long (2013) conducted a thorough investigation of frequency-dependent shear wave splitting beneath NNA, and suggested the presence of (at least) two anisotropic layers. The upper layer is likely either above or within the slab and displays a trench-oblique (to trench-subparallel) fast orientation, while the lower layer is likely beneath the slab and displays a trench normal fast orientation. These layers may contribute to the anisotropic characteristics of some of our inferred interfaces (specifically those at 6.8 s, 9.6 s, and/or 12 s) (Fig. 9 in Eakin and Long, 2013). Eakin et al. (2014) analyzed shear wave splitting from local S phases beneath the PULSE array and suggested that a likely source of the anisotropy sampled by their data is the mantle wedge material between the overriding continent and the subducting slab. They further correlate this mantle wedge anisotropy with the upper layer suggested in the two-layer model of frequency-dependent SKS splitting beneath NNA (Eakin and Long, 2013). We suggest that the anisotropic interface visible on our RF gathers at a delay time of 6.8 s and/or 7.5 s may correspond to either the top or bottom of this layer. In any case, our results suggest that there are more than two anisotropic layers beneath NNA. A comparison between our RF results beneath Peru and the azimuthally anisotropic Rayleigh wave phase velocity maps of Antonijevic et al. (2016) reveal some qualitative similarities, in that there is some variability in fast orientation with period beneath NNA and the surrounding region. However, a direct comparison between the two types of observations is difficult, because phase velocity maps at individual periods average structure over a depth range that depends on period.

5.4. Layered crustal anisotropy beneath the Andes: implications for crustal deformation during orogenesis

A significant finding of this study is the presence of multiple interfaces within the continental crust whose characteristics require a sharp gradient in seismic anisotropy with depth, particularly beneath LPAZ in northern Bolivia. Our finding of complex, multilayered anisotropy within the thick Andean crust is consistent with recent observations of strong radial anisotropy in the mid-crust beneath the Andes (Lynner et al., 2018) and similar to recent observations in other modern orogenic settings, including the Tibetan Plateau (Liu et al., 2015) and Taiwan (Huang et al., 2015), and in ancient orogens such as the Appalachians (Long et al., 2017). Specifically, Liu et al. (2015) applied anisotropic RF analysis to stations in Tibet and found evidence for similarly complex anisotropy; they invoked viscous flow in the middle-to-lower crust, along with a contribution from the SPO of metamorphic fluids, as an explanation for their observations. Huang et al. (2015) applied ambient noise tomography of crustal structure to data from Taiwan and found evidence for a sharp change in anisotropy with depth in the mid-crust (~10–15 km), suggesting a change in the geometry of crustal deformation with depth associated with compression, shortening, and mountain building. Long et al. (2017) found evidence for layered crustal anisotropy beneath seismic stations in the Appalachian Mountains and pointed out similarities between these structures and those in modern orogens.

Taken together with these recent studies, our results beneath the Andes point to complex deformation of the entire crustal column during the mountain building process, with sharp vertical gradients in the geometry of deformation, the mechanism for anisotropy, the rheology of the crust, or a combination of these. Given recent and ongoing progress in our understanding of how to relate deformation to anisotropy in various crustal mineral assemblages (e.g., Almqvist and Mainprice, 2017; Brownlee et al., 2017), observations of layered crustal anisotropy in orogenic settings may eventually lead to a detailed and quantitative understanding of how deformation is accommodated throughout the crust during orogenesis. In the specific context of the Andes, our finding of significant anisotropy throughout the crust, likely including its deepest portions, may lend support to the idea of pervasive crustal deformation as a mechanism for crustal thickening (e.g., Eichelberger et al., 2015; Lynner et al., 2018). While our observations suggesting that anisotropy is distributed across a range of depths within the crust are consistent with this idea, it is also true that our observations require the presence of sharp contrasts in anisotropy with depth, which suggests the possible presence of localized features such as shear zones.

5.5. Towards the integration of multiple constraints on anisotropy beneath Peru and Bolivia

The RF analysis presented in this study establishes unequivocal evidence for the presence of layered anisotropy within the crust and uppermost mantle beneath southern Peru and northern Bolivia. Our analysis constrains some structural features such the depth of dipping and anisotropic-contrast interfaces, along with some information about the orientation of the dip direction or the anisotropic symmetry axes. This type of analysis, however, does not provide the precise geometry of

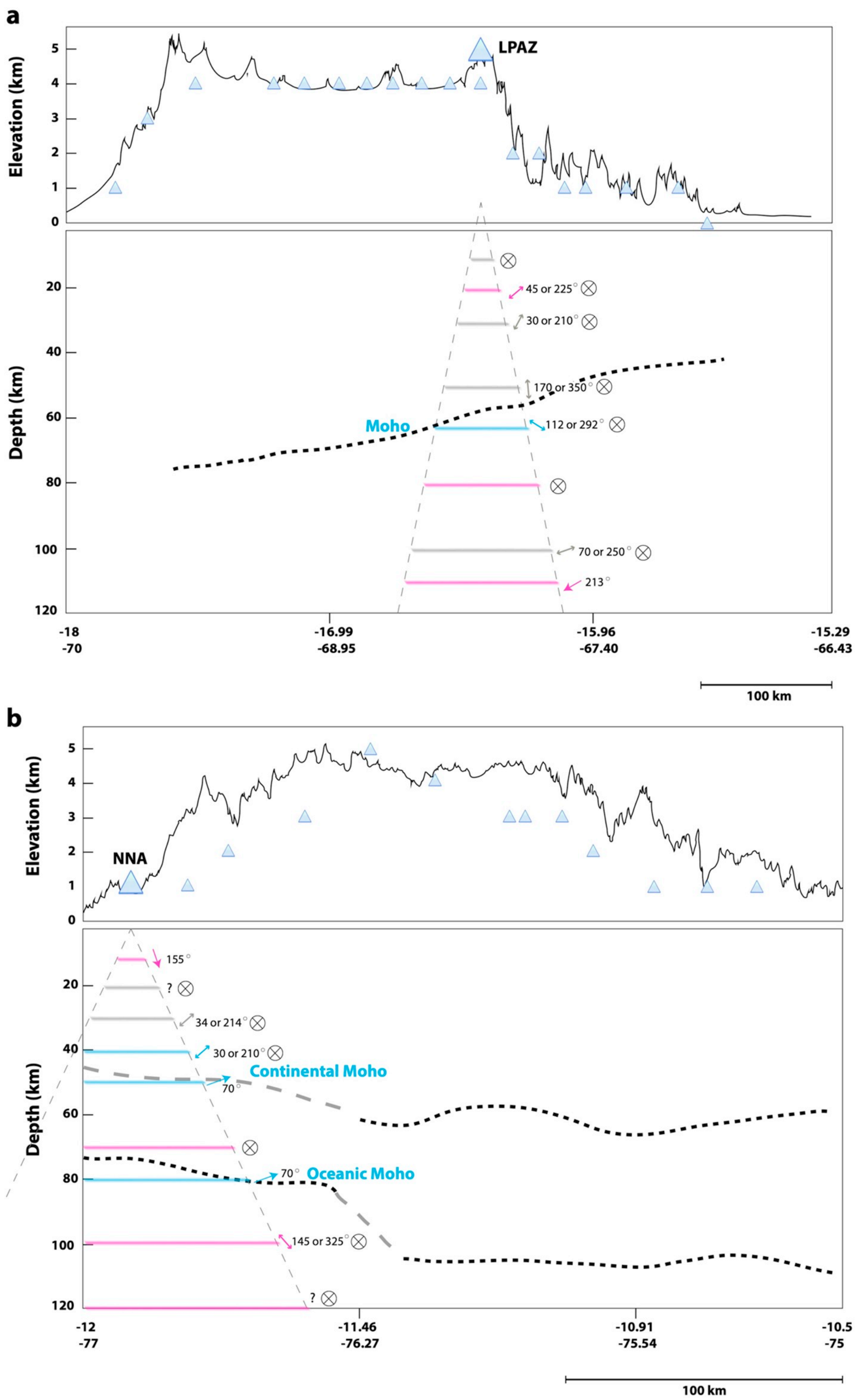

Fig. 12. Interpretive cartoon of inferred structures for both LPAZ and NNA. (a) The inferred structure beneath LPAZ station shown along the CAUGHT array cross-section. The dashed black line is the inferred Moho based on Ryan et al. (2016) (their Fig. 5). LPAZ station is marked by the bigger triangle, whereas the rest of the triangles mark the CAUGHT array stations analyzed in this study. The colored lines are showing the Moho (cyan) and other major interfaces discussed in the text and shown in Figs. 4–5. The gray lines mark positive picks and magenta lines mark negative ones (similar colour scheme as in the previous figures). The arrows next to the colored lines indicate a dipping interface (one head) or a plunging symmetry axis (2 arrow heads), based on RF and HD analysis; the numbers next to the arrows are the inferred tilt directions based on HD direction analysis. The circles with Xs indicate interfaces with a contrast in azimuthal anisotropy, either associated with a plunge (adjacent to an arrow) or close to horizontal. The dotted gray cone represents the incidence angles. (b) The inferred structure beneath NNA station shown along the PULSE array cross-section. The dashed black lines are the inferred Mohos based on Bishop et al. (2017) (their Fig. 3c), whereas the gay parts are inferred rather than clearly visible in their CCP stack analysis. NNA station is marked by the bigger triangle, whereas the rest of the triangles mark the PULSE array stations analyzed in this study. The cyan lines mark the two options inferred for the continental Moho (see Section 4.3). The gray lines (positive picks) and magenta lines (negative picks) mark other major interfaces discussed in the text and shown in Figs. 9–10. The arrows next to the colored lines indicate a dipping interface (one head) or a plunging symmetry axis (2 arrow heads) (based on RF and HD analysis); the numbers next to the arrows are the inferred tilt directions based on HD direction analysis. The circles with Xs indicate interfaces with a contrast in azimuthal anisotropy, either associated with a plunge (adjacent to an arrow), or close to horizontal, or associated with complicated patterns (adjacent to a question mark). Note that the incidence angle in (b) appears different than in (a) because of the different horizontal scale. (For interpretation of the references to colour in this figure legend, the reader is referred to the web version of this article.)

anisotropy within each layer (for additional discussion of this point, see Ford et al., 2016). Specifically, our analysis does not resolve whether the upper layer, lower layer, or both layers surrounding an interface are anisotropic. Detailed forward modeling of receiver function data that explicitly considers the anisotropic geometry of each layer is feasible, but highly non-unique (e.g., Wirth et al., 2017). Our results, therefore, should be viewed in the context of the full suite of seismic observations that can constrain seismic anisotropy at depth. Different methodologies for observing seismic anisotropy, including shear wave splitting, surface wave tomography, and anisotropy-aware RF analysis, are complementary and provide different resolving power, both laterally and with depth. Further progress on characterizing the three-dimensional distribution of seismic anisotropy in complex regions such as Peru and Bolivia is likely to come via the integration, and hopefully eventually the joint inversion, of constraints from multiple methods of measuring anisotropy (e.g., Yuan and Levin, 2014). Abundant observations of seismic anisotropy beneath Peru and Bolivia are now available, including results from this study and from previous work (Antonijevic et al., 2016; Eakin and Long, 2013; Eakin et al., 2014, 2015; Long et al., 2016). Furthermore, there is potential to add additional observations from analyses such as Pn tomography (e.g., Buehler and Shearer, 2010) or Love-to-Rayleigh wave scattering (e.g., Rieger and Park, 2010) applied to PULSE and CAUGHT data. This region of the South American subduction zone is thus poised for future progress on the joint interpretation of multiple observations to untangle its complex anisotropic structure.

6. Summary

We carried out anisotropy-aware RF analysis using data from southern Peru and northern Bolivia, including permanent stations NNA and LPAZ and stations from the PULSE and CAUGHT temporary deployments. We computed radial and transverse component RFs as a function of backazimuth, and we also carried out visual inspection of transverse component RF rose plots and harmonic decomposition modeling. We identified the Moho of the continental upper plate (and, beneath Peru, the Moho of the subducting slab) and found evidence for laterally variable, multi-layer anisotropy, as well as dipping interfaces, underneath both regions. Our results are generally compatible with previous RF studies in the region, but our consideration of transverse component RFs and their variation with backazimuths adds important spatial information to previous isotropic RFs analysis. Our documentation of multiple layers of anisotropy within the crust, particularly beneath LPAZ, lends support to the idea of pervasive deformation of the entire crustal column during orogenesis, and is similar to observations in other modern and ancient orogenic systems. While our analysis cannot completely characterize the geometry of anisotropy within each layer of the crust and upper mantle, the combination of constraints from anisotropy-aware RF analysis with other methods of measuring anisotropy, including shear wave splitting and surface wave tomography, holds potential for future detailed modeling of the three-dimensional distribution of anisotropy beneath Peru and Bolivia.

Acknowledgements

Data used in this study were downloaded from the Incorporated Research Institutions for Seismology (IRIS) Data Management Center (DMC) at http://ds.iris.edu. Seismic instruments and support for the CAUGHT and PULSE experiments were provided by the IRIS PASSCAL Instrument Center at New Mexico Tech. The facilities of the IRIS Consortium are supported by the National Science Foundation (NSF) under Cooperative Agreement EAR-1261681 and the DOE National Nuclear Security Administration. This work was supported by NSF grants EAR-0943962 (MDL), EAR-0944181 and EAR-0908777 (LSW), EAR-0943991 (SLB), and EAR-0907880 (SLB and GZ), as well as by Yale University. We are grateful to Jeffrey Park and Heather Ford for sharing analysis codes and for helpful advice. Finally, we thank the anonymous reviewers for detailed and constructive comments that helped us to improve the paper.

Appendix A. Supplementary data

Supplementary data to this article can be found online at https://doi.org/10.1016/j.tecto.2019.01.007.

References

Almqvist, B.S.G., Mainprice, D., 2017. Seismic properties and anisotropy of the continental crust: predictions based on mineral texture and rock microstructure. Rev. Geophys. 55, 367–433. https://doi.org/10.1002/2016RG000552.

Antonijevic, S.K., Wagner, L.S., Kumar, A., Beck, S.L., Long, M.D., Zandt, G., Tavera, H., Condori, C., 2015. The role of ridges in the formation and longevity of flat slabs. Nature 524, 212–215. https://doi.org/10.1038/nature14648.

Antonijevic, S.K., Wagner, L.S., Beck, S.L., Long, M.D., Zandt, G., Tavera, H., 2016. Effects of change in slab geometry on the mantle flow and slab fabric in Southern Peru. J. Geophys. Res. 121, 7252–7270. https://doi.org/10.1002/2016JB013064.

Bianchi, I., Park, J., Piana Agostinetti, N., Levin, V., 2010. Mapping seismic anisotropy using harmonic decomposition of receiver functions: an application to Northern Apennines, Italy. J. Geophys. Res. 115, B12317. https://doi.org/10.1029/2009JB007061.

Bishop, B.T., Beck, S.L., Zandt, G., Wagner, L., Long, M., Antonijevic, S.K., Kumar, A., Tavera, H., 2017. Causes and consequences of flat-slab subduction in southern Peru. Geosphere 13, 1392–1407.

Bishop, B.T., Beck, S.L., Zandt, G., Wagner, L.S., Long, M.D., Tavera, H., 2018. Foreland uplift during flat subduction: Insights from the Peruvian Andes and Fitzcarrald Arch. Tectonophysics 731–732, 73–84.

Bostock, M.G., 1998. Mantle stratigraphy and evolution of the Slave province. J. Geophys. Res. 103, 21,183–21,200. https://doi.org/10.1029/98JB01069.

Brownlee, S.J., Schulte-Pelkum, V., Raju, A., Mahan, K., Condit, C., Orlandini, O.F., 2017. Characteristics of deep crustal seismic anisotropy from a compilation of rock elasticity tensors and their expression in receiver functions. Tectonics 36, 1835–1857. https://doi.org/10.1002/2017TC004625.

Buehler, J.S., Shearer, P.M., 2010. Pn tomography of the western United States using USArray. J. Geophys. Res. 115, B09315. https://doi.org/10.1029/2009JB006874.

Cahill, T., Isacks, B.L., 1992. Seismicity and shape of the subducted Nazca plate. J. Geophys. Res. 97, 17503–17529.

Dougherty, S.L., Clayton, R.W., 2014. Seismic structure in southern Peru: evidence for a smooth contortion between flat and normal subduction of the Nazca Plate. Geophys. J. Int. 200, 534–555.

Eakin, C.M., Long, M.D., 2013. Complex anisotropy beneath the Peruvian flat slab from frequency-dependent, multiple-phase shear wave splitting analysis. J. Geophys. Res. 118, 4794–4813. https://doi.org/10.1002/jgrb.50349.

Eakin, C.M., Long, M.D., Beck, S.L., Wagner, L.S., Tavera, H., Condori, C., 2014. Response of the mantle to flat slab evolution: Insights from local S splitting beneath Peru. Geophys. Res. Lett. 41, 3438–3446.

Eakin, C.M., Long, M.D., Wagner, L.S., Beck, S.L., Tavera, H., 2015. Upper mantle anisotropy beneath Peru from SKS splitting: Constraints on flat slab dynamics and interaction with the Nazca Ridge. Earth Planet. Sci. Lett. 412, 152–162.

Eichelberger, N., McQuarrie, N., Ryan, J., Karimi, B., Beck, S., Zandt, G., 2015. Evolution of crustal thickening in the central Andes, Bolivia. Earth Planet. Sci. Lett. 426, 191–203.

Erslev, E.A., 2005. 2D Laramide geometries and kinematics of the Rocky Mountains, western USA. In: The Rocky Mountain Region: An Evolving Lithosphere Tectonics, Geochemistry, and Geophysics, pp. 7–20.

Ford, H.A., Long, M.D., Wirth, E.A., 2016. Midlithospheric discontinuities and complex anisotropic layering in the mantle lithosphere beneath the Wyoming and Superior Provinces. J. Geophys. Res. 121, 6675–6697. https://doi.org/10.1002/2016JB012978.

Garzione, C.N., Molnar, P., Libarkin, J.C., MacFadden, B.J., 2006. Rapid late Miocene rise of the Bolivian Altiplano: evidence for removal of mantle lithosphere. Earth Planet. Sci. Lett. 241, 543–556.

Garzione, C.N., Hoke, G.D., Libarkin, J.C., Withirs, S., MacFadden, B., Eiler, J., Ghosh, P., Mulch, A., 2008. Rise of the Andes. Science 320, 1304–1307.

Garzione, C.N., McQuarrie, N., Perez, N.D., Ehlers, T.A., Beck, S.L., Kar, N., Eichelberger, N., Chapman, A.D., Ward, K.M., Ducea, M.N., Lease, R.O., Poulsen, C.J., Wagner, L.S., Saylor, J.E., Zandt, G., Horton, B.K., 2017. Tectonic evolution of the Central Andean Plateau and implications for the growth of plateaus. Annu. Rev. Earth Planet. Sci. 45, 529–559.

Gutscher, M.-A., Olivet, J.-L., Aslanian, D., Eissen, J.-P., Maury, R., 1999. The “lost Inca Plateau”: cause of flat subduction beneath Peru? Earth Planet. Sci. Lett. 171, 335–341.

Gutscher, M., Spakman, W., Bijwaard, H., Engdahl, E., 2000. Geodynamics of flat subduction: seismicity and tomographic constraints from the Andean margin. Tectonics 19, 814–833.

Hayes, G.P., Wald, D.J., Johnson, R.L., 2012. Slab1.0: a three-dimensional model of global subduction zone geometries. J. Geophys. Res. 117, B01302. https://doi.org/10.1029/2011JB008524.

Helffrich, G., 2006. Extended-time multitaper frequency domain cross-correlation receiver-function estimation. Bull. Seismol. Soc. Am. 96, 344–347.

Huang, T.-Y., Gung, Y., Kuo, B.-Y., Chiao, L.-Y., Chen, Y.-N., 2015. Layered deformation in the Taiwan orogeny. Science 349, 720–723. https://doi.org/10.1126/science.aab1879.

Isacks, B.L., 1988. Uplift of the central Andean plateau and bending of the Bolivian orocline. J. Geophys. Res. 93, 3211–3231.

Jones, C.H., Phinney, R.A., 1998. Seismic structure of the lithosphere from teleseismic converted arrivals observed at small arrays in the southern Sierra Nevada and vicinity, California. J. Geophys. Res. Solid Earth 103 (B5), 10065–10090.

Jordan, T.E., Allmendinger, R.W., 1986. The Sierras Pampeanas of Argentina; a modern analogue of Rocky Mountain foreland deformation. Am. J. Sci. 286, 737–764.

Kennett, B.L.N., Engdahl, E.R., Buland, R., 1995. Constraints on seismic velocities in the Earth from traveltimes. Geophys. J. Int. 122, 108–124.

Kreemer, C., Blewitt, G., Klein, E.C., 2014. A geodetic plate motion and Global Strain Rate Model. Geochem. Geophys. Geosyst. 15, 3849–3889. https://doi.org/10.1002/2014GC005407.

Kumar, A., Wagner, L.S., Beck, S.L., Long, M.D., Zandt, G., Young, B., Tavera, H., Minaya, E., 2016. Seismicity and state of stress in the central and southern Peruvian flat slab. Earth Planet. Sci. Lett. 441, 71–80. https://doi.org/10.1016/j.epsl.2016.02.023.

Lamb, S., Hoke, L., 1997. Origin of the high plateau in the Central Andes, Bolivia, South America. Tectonics 16, 623–649.

Levin, V., Park, J., 1997. P-SH conversions in a flat-layered medium with anisotropy of arbitrary orientation. Geophys. J. Int. 131, 253–266.

Liu, Z., Park, J., 2016. Seismic receiver function interpretation: Ps splitting or anisotropic underplating? Geophys. J. Int. 208, 1332–1341.

Liu, Z., Park, J., Rye, D.M., 2015. Crustal anisotropy in northeastern Tibetan Plateau inferred from receiver functions: rock textures caused by metamorphic fluids and lower crust flow? Tectonophysics 661, 66–80.

Long, M.D., 2013. Constraints on subduction geodynamics from seismic anisotropy. Rev.

Geophys. 51, 76–112. https://doi.org/10.1002/rog.20008.

Long, M.D., Becker, T.W., 2010. Mantle dynamics and seismic anisotropy. Earth Planet. Sci. Lett. 297, 341–354.

Long, M.D., Biryol, C.B., Eakin, C.M., Beck, S.L., Wagner, L.S., Zandt, G., Minaya, E., Tavera, H., 2016. Overriding plate, mantle wedge, slab, and subslab contributions to seismic anisotropy beneath the northern Central Andean Plateau. Geochem. Geophys. Geosyst. 17, 2556–2575.

Long, M.D., Ford, H.A., Abrahams, L., Wirth, E.A., 2017. The seismic signature of lithospheric deformation beneath eastern North America due to Grenville and Appalachian orogenesis. Lithosphere 9, 987–1001.

Lynner, C., Beck, S.L., Zandt, G., Porritt, R.W., Lin, F.-C., Eilon, Z.C., 2018. Midcrustal deformation in the Central Andes constrained by radial anisotropy. J. Geophys. Res. 123. https://doi.org/10.1029/2017JB014936.

Mamani, M., Wörner, G., Sempere, T., 2010. Geochemical variations in igneous rocks of the Central Andean orocline (13 S to 18 S): tracing crustal thickening and magma generation through time and space. Bulletin 122 (1–2), 162–182.

McCormack, K., Wirth, E.A., Long, M.D., 2013. B-type olivine fabric and mantle wedge serpentinization beneath the Ryukyu arc. Geophys. Res. Lett. 40, 1697–1702. https://doi.org/10.1002/grl.50369.

McQuarrie, N., Barnes, J.B., Ehlers, T.A., 2008. Geometric, kinematic, and erosional history of the central Andean Plateau, Bolivia (15–17 S). Tectonics 27.

Menke, W., 2012. Geophysical Data Analysis: Discrete Inverse Theory. Academic Press, Amsterdam, The Netherlands (293 pp).

Olugboji, T.M., Park, J., 2016. Crustal anisotropy beneath Pacific Ocean islands from harmonic decomposition of receiver functions. Geochem. Geophys. Geosyst. 17, 810–832. https://doi.org/10.1002/2015GC006166.

Owens, T.J., Crotwell, H.P., Groves, C., Oliver-Paul, P., 2004. SOD: Standing order for data. Seismol. Res. Lett. 75, 515–520. https://doi.org/10.1785/gssrl.75.4.515-a.

Park, J., Levin, V., 2000. Receiver functions from multiple-taper spectral correlation estimates. Bull. Seismol. Soc. Am. 90, 1507–1520.

Park, J., Levin, V., 2016. Anisotropic shear zones revealed by backazimuthal harmonics of teleseismic receiver functions. Geophys. J. Int. 207, 1216–1243.

Park, J., Levin, V., Brandon, M., Lees, J., Peyton, V., Gordeev, E., Ozerov, A., 2002. A Dangling Slab, Amplified Arc Volcanism, Mantle Flow and Seismic Anisotropy in the Kamchatka Plate Corner. Plate Boundary Zones. pp. 295–324.

Park, J., Yuan, H., Levin, V., 2004. Subduction zone anisotropy beneath Corvallis, Oregon: a serpentinite skid mark of trench-parallel terrane migration? J. Geophys. Res. 109, B10306. https://doi.org/10.1029/2003JB002718.

Rieger, D.M., Park, J., 2010. USArray observations of quasi-Love surface wave scattering: orienting anisotropy in the Cascadia plate boundary. J. Geophys. Res. 115, B055306. https://doi.org/10.1029/2009JB006754.

Ryan, J., Beck, S., Zandt, G., Wagner, L., Minaya, E., Tavera, H., 2016. Central Andean crustal structure from receiver function analysis. Tectonophysics 682, 120–133.

Savage, M.K., 1998. Lower crustal anisotropy or dipping boundaries? Effects on receiver functions and a case study in New Zealand. J. Geophys. Res. Solid Earth 103 (B7), 15069–15087.

Savage, M.K., 1999. Seismic anisotropy and mantle deformation: what have we learned from shear wave splitting? Rev. Geophys. 37, 65–106.

Schulte-Pelkum, V., Mahan, K.H., 2014. A method for mapping crustal deformation and anisotropy with receiver functions and first results from USArray. Earth Planet. Sci. Lett. 402, 221–233.

Scire, A., Zandt, G., Beck, S., Long, M., Wagner, L., Minaya, E., Tavera, H., 2016. Imaging the transition from flat to normal subduction: variations in the structure of the Nazca slab and upper mantle under southern Peru and northwestern Bolivia. Geophys. J. Int. 204, 457–479.

Shiomi, K., Park, J., 2008. Structural features of the subducting slab beneath the Kii Peninsula, central Japan: Seismic evidence of slab segmentation, dehydration, and anisotropy. J. Geophys. Res. 113, B10318. https://doi.org/10.1029/2007JB005535.

Silver, P.G., Chan, W.W., 1991. Shear wave splitting and subcontinental mantle deformation. J. Geophys. Res. 96 (B10), 16429–16454.

Ward, K.M., Zandt, G., Beck, S.L., Wagner, L.S., Tavera, H., 2016. Lithospheric structure beneath the northern Central Andean Plateau from the joint inversion of ambient noise and earthquake-generated surface waves. J. Geophys. Res. Solid Earth 121, 8217–8238. https://doi.org/10.10029/2016JB013237.

Wirth, E.A., Long, M.D., 2012. Multiple layers of seismic anisotropy and a low-velocity region in the mantle wedge beneath Japan: evidence from teleseismic receiver functions. Geochem. Geophys. Geosyst. 13, Q08005. https://doi.org/10.1029/2012GC004180.

Wirth, E.A., Long, M.D., 2014. A contrast in anisotropy across mid-lithospheric discontinuities beneath the central United States—a relic of craton formation. Geology 42, 851–854.

Wirth, E.A., Long, M.D., Moriarty, J.C., 2017. A Markov chain Monte Carlo with Gibbs sampling approach to anisotropic receiver function forward modeling. Geophys. J. Int. 208, 10–13. https://doi.org/10.1093/gji/ggw383.

Yuan, H., Levin, V., 2014. Stratified seismic anisotropy and the lithosphere-asthenosphere boundary beneath eastern North America. J. Geophys. Res. Solid Earth 119, 3096–3114. https://doi.org/10.1002/2013JB010785.